EFFECT OF HOT ISOSTATIC PRESSING ON DENSIFICATION, MICROSTRUCTURE, AND ELECTRICAL PROPERTIES OF $0.95MgTiO_3$-$0.05CaTiO_3$ CERAMIC

A THESIS SUBMITTED TO
THE GRADUATE SCHOOL OF NATURAL AND APPLIED SCIENCES
OF
MIDDLE EAST TECHNICAL UNIVERSITY

BY

SELİN GÜNTOP

IN PARTIAL FULFILLMENT OF THE REQUIREMENTS
FOR
THE DEGREE OF MASTER OF SCIENCE
IN
METALLURGICAL AND MATERIALS ENGINEERING

JANUARY 2023

Approval of the thesis:

EFFECT OF HOT ISOSTATIC PRESSING ON DENSIFICATION, MICROSTRUCTURE, AND ELECTRICAL PROPERTIES OF $0.95MgTiO_3$-$0.05CaTiO_3$ CERAMIC

submitted by **SELİN GÜNTOP** in partial fulfillment of the requirements for the degree of **Master of Science** i**n Metallurgical and Materials Engineering, Middle East Technical University** by,

Prof. Dr. Halil Kalıpçılar
Dean, Graduate School of **Natural and Applied Sciences** _____

Prof. Dr. Ali Kalkanlı
Head of the Department, **Met. And Mat. Eng.** _____

Prof. Dr. Abdullah Öztürk
Supervisor, **Met. And Mat. Eng., METU** _____

Examining Committee Members:

Prof. Dr. Caner Durucan
Metallurgical and Materials Eng., METU _____

Prof. Dr. Abdullah Öztürk
Metallurgical and Materials Eng., METU _____

Prof. Dr. Cihangir Duran
Metallurgical and Materials Eng., Ankara Yıldırım Beyazıt Uni. _____

Prof. Dr. Jongee Park
Metallurgical and Materials Eng., Atılım Uni. _____

Assist. Prof. Dr. Yusuf Keleştemur
Metallurgical and Materials Eng., METU _____

Date: 20.01.2023

I hereby declare that all information in this document has been obtained and presented in accordance with academic rules and ethical conduct. I also declare that, as required by these rules and conduct, I have fully cited and referenced all material and results that are not original to this work.

Name Last name: Selin Güntop

Signature:

ABSTRACT

EFFECT OF HOT ISOSTATIC PRESSING ON DENSIFICATION, MICROSTRUCTURE, AND ELECTRICAL PROPERTIES OF $0.95MgTiO_3$-$0.05CaTiO_3$ CERAMIC

Güntop, Selin
Master of Science, Metallurgical and Materials Engineering
Supervisor: Prof. Dr. Abdullah Öztürk

January 2023, 88 pages

The effect(s) of hot isostatic pressing (HIPing) on densification, microstructure, and electrical properties of pressureless sintered $0.95MgTiO_3$-$0.05CaTiO_3$ (M0.95CT) ceramic was researched. M0.95CT ceramic was prepared by the mixed oxide method. The powder mixture of the oxide components in appropriate molar ratios was compacted in a stainless steel die by uniaxial action pressing. The square shaped compacts with nominal dimensions of 35 mm in size and 4 mm in thickness were pressureless sintered in air at temperatures of 1300, 1350, and 1400 ^{o}C for 1 h. The M0.95CT ceramic pressureless sintered at 1400 ^{o}C had 96.06% relative density. HIPing was applied at 1200 ^{o}C for 1 h only to the M0.95CT ceramic pressureless sintered at 1400 ^{o}C . The effects of HIPing on the characteristics and electrical properties of M0.95CT ceramic was evaluated on the samples produced by application of HIP and without HIP. Results revealed that HIPing has a profound influence on densification, microstructural development, and electrical properties especially on insulating behavior of M0.95CT ceramic.

Keywords: $0.95MgTiO_3$-$0.05CaTiO_3$ ceramic, mixed oxide method, hot isostatic pressing, microstructure, electrical properties

ÖZ

SICAK İZOSTATİK PRESLEMENİN $0.95MgTiO_3$-$0.05CaTiO_3$ SERAMİĞİNİN YOĞUNLAŞMASI, MİKRO YAPISI, VE ELEKTRİKSEL ÖZELLİKLERİNE ETKİSİ

Güntop, Selin
Yüksek Lisans, Metalurji ve Malzeme Mühendisliği
Tez Yöneticisi: Prof. Dr. Abdullah Öztürk

Ocak 2023, 88 sayfa

Sıcak izostatik preslemenin (HIP) $0.95MgTiO_3$-$0.05CaTiO_3$ (M0.95CT) seramiğinin yoğunlaşması, mikroyapısı, ve elektriksel özellikleri üzerindeki etkileri araştırıldı. M0.95CT seramiği, geleneksel oksit karışımları yöntemiyle hazırlandı. Oksit bileşenlerinin uygun molar oranlarda toz karışımı, tek yönlü presleme ile paslanmaz çelik bir kalıpta sıkıştırıldı. Nominal boyutları 35 mm, kalınlığı 4 mm olan kare şeklindeki kompaktlar 1300, 1350 ve 1400 ^{o}C'de havada 1 saat basınçsız sinterlendi. 1400 ^{o}C 'de basınçsız sinterlenen M0.95CT seramiği, %96.06 bağıl yoğunluk göstermiştir. HIP sadece 1400 ^{o}C 'de basınçsız sinterlenen M0.95CT seramiğine 1200 ^{o}C'de 1 saat uygulandı. HIP uygulamasının M0.95CT seramiğinin karakteristiklerine ve elektriksel özelliklerine etkileri, HIP uygulanmış ve HIP uygulanmamış numuneler üzerinden değerlendirilmiştir. Sonuçlar, HIP uygulamasının M0.95CT seramiğinin yoğunlaşması, mikroyapısal gelişimi, ve elektriksel özelliklerine özellikle yalıtkan davranışı üzerinde ciddi etkilerinin olduğunu ortaya koydu.

Anahtar Kelimeler: $0.95MgTiO_3$-$0.05CaTiO_3$ ceramic, oksit karışımları yöntemi, sıcak izostatik presleme, mikroyapı, elektriksel özellikler

To my dear family

ACKNOWLEDGMENTS

I would like to express my deepest appreciation to my supervisor, Prof. Dr. Abdullah Öztürk for his guidance, invaluable patience, and feedback.

I owe special thanks to Prof. Dr. Alpagut Kara, Prof. Dr. Sedat Ballıkaya, Assoc. Prof. Dr. Volkan Kalem, and Prof. Dr. Ahmet Macit Özenbaş, who generously provided knowledge and expertise.

I would also like to thank Dr. Necmettin Kaan Çalışkan, Dr. Mehmet Kaan Pehlivanoğlu, and Hakan Der for their guidance, advice and encouragements through the research.

Thanks should also go to TUBITAK SAGE, who provided financial and technical device support for my research.

I also could not have undertaken this journey without my office mates for their editing help and moral support.

I am also grateful to ROKO team for all the entertainment and for believing in me.

Lastly, and most importantly, I would like to especially thank my family. Their belief in me has kept my spirits and motivation high during this process.

TABLE OF CONTENTS

ABSTRACT v

ÖZ vii

ACKNOWLEDGMENTS x

TABLE OF CONTENTS xi

LIST OF TABLES xiv

LIST OF FIGURES xv

LIST OF ABBREVIATIONS xviii

CHAPTERS

1 INTRODUCTION 1

2 LITERATURE REVIEW 5

2.1 $MgTiO_3$- $CaTiO_3$ Ceramics 5

2.2 Dielectric Mechanisms 8

2.3 Dielectric Constant and Loss 11

2.4 Mixed Oxide Method 13

2.5 Hot Isostatic Pressing (HIPing) 15

2.6 Resistivity 17

2.7 Hall Effect 18

2.8 Absorbance 20

3 EXPERIMENTAL PROCEDURE 23

3.1 Sample Preparation 23

3.2 Characterization 29

3.2.1 X-Ray Diffraction (XRD) Analysis 29

3.2.2 Scanning Electron Microscopy (SEM) Analysis 29
3.2.3 Energy Dispersive Spectroscopy (EDS) Analysis 29
3.2.4 Particle Size Analysis 30
3.3 Property Measurement 30
3.3.1 Density 30
3.3.2 Dielectric Constant and Dielectric Loss 31
3.3.3 Resistivity 32
3.3.4 Hall Effect 32
3.3.5 Absorbance 33
4 RESULTS AND DISCUSSION 35
4.1 Characterization of Starting Powders 35
4.1.1 Particle Size Analysis 35
4.1.2 X-Ray Diffraction (XRD) Analysis 37
4.1.3 SEM Analysis 40
4.1.4 EDS Analysis 43
4.2 Characterization of the Calcined M0.95CT Powder 46
4.2.1 Particle Size Analysis 46
4.2.2 XRD Analysis 47
4.3 Effect of Green Density 50
4.4 Sintering of M0.95CT Ceramics 53
4.4.1 Characterization of Pressureless Sintered M0.95CT Ceramic 53
4.4.2 Characterization of M0.95CT-HIP Ceramic 59
4.4.3 Properties of Pressureless Sintered M0.95CT Ceramics 62
4.4.4 Properties of M0.95CT-HIP Ceramics 68

5 CONCLUSION 77
6 FUTURE STUDIES 79
REFERENCES 80

LIST OF TABLES

TABLES

Table 1. Powders used in the production of M0.95CT ceramics. 23

Table 2. EDS analysis of the thermally etched M0.95CT ceramic pressureless sintered at 1400 °C. The analysis was done at different points shown in Figure 36. 59

LIST OF FIGURES

FIGURES

Figure 1. $MgO-TiO_2$ phase diagram. [20] 6
Figure 2. $CaO-TiO_2$ phase diagram. [21] 7
Figure 3. $MgTiO_3$- $CaTiO_3$ binary phase diagram. [19] 7
Figure 4. Schematics of (a) atomic, (b) ionic, (c) dipole, and (d) space charge polarization mechanisms. [25] 9
Figure 5. Variation of dielectric constant with frequency. [28] 10
Figure 6. Parallel plate capacitor schema (DC case). [27] 11
Figure 7. Loss tangent vector schema. [27] 12
Figure 8. Flow chart showing the main steps involved in the production of polycrystalline ceramics. [29] 14
Figure 9. HIPing of Si_3N_4 ceramics. [35] 15
Figure 10. The four-point probe approach schema. [37] 18
Figure 11. Hall-Effect Measurement Schema. [37] 19
Figure 12. Different configurations for Hall effect measurements: (A) Hall bar; (B) Hall bar with contact arms; (C) Square; (D) Greek cross, (E) Circle; (F) Cloverleaf. [37] 20
Figure 13. Calcination schedule. 24
Figure 14. Sintering schedule for M0.95CT ceramic. 26
Figure 15. M0.95CT ceramic pellets; (a) pressureless sintered at 1400 °C, and (b) HIPed at 1200 °C. 26
Figure 16. HIPing schedule for M0.95CT-HIP ceramic. 27
Figure 17. The process flow diagram including the steps used in the production of M0.95CT and M0.95CT-HIP ceramics. 28
Figure 18. Particle size distribution histogram of the MgO starting powder. 35
Figure 19. Particle size distribution histogram of the $CaCO_3$ starting powder. 36
Figure 20. Particle size distribution histogram of the TiO_2 starting powder. 37
Figure 21. XRD pattern of the MgO starting powder. 38

Figure 22. XRD pattern of the TiO_2 starting powder. 39
Figure 23. XRD pattern of the $CaCO_3$ starting powder..... 40
Figure 24. SEM images of the (a) MgO, (b) TiO_2, and (c) $CaCO_3$ starting powders. (1000 X)..... 42
Figure 25. EDS spectrum of the MgO starting powder. The EDS analysis was taken at the spot shown in red color in the SEM image..... 43
Figure 26. EDS spectrum of the TiO_2 starting powder. The EDS analysis was taken at the spot shown in red color in the SEM image..... 44
Figure 27. EDS spectrum of the $CaCO_3$ starting powder. The EDS analysis was taken at the spot shown in red color in the SEM image. 45
Figure 28. Particle size distribution histogram of the M0.95CT powder..... 46
Figure 29. XRD patterns of M0.95CT powder..... 48
Figure 30. XRD patterns of M0.95CT ceramic. The patterns were taken after the 1st calcination, 2nd calcination, and pressureless sintering at 1400 °C. 50
Figure 31. Variation in the relative green density with applied pressure..... 51
Figure 32. Variation in shrinkage occurred during sintering at M0.95CT ceramic with applied pressure..... 52
Figure 33. XRD patterns of the M0.95CT ceramic pressureless sintered at 1300, 1350, and 1400 °C. 54
Figure 34. SEM images of the thermally etched M0.95CT ceramics pressureless sintered at (a) 1300, (b) 1350, and (c) 1400 °C. (2500 X) 56
Figure 35. SEM image of the thermally etched M0.95CT ceramic pressureless sintered at 1400 °C. (1250 X)..... 57
Figure 36. BSD-SEM image of the thermally etched M0.95CT ceramic pressureless sintered at 1400 °C. 58
Figure 37. XRD patterns taken before and after the application of HIPing for the M0.95CT ceramic pressureless sintered at 1400 °C..... 60
Figure 38. SEM images taken (a) before and (b) after the application of HIPing for the M0.95CT ceramics pressureless sintered at 1400 °C. (2000 X)..... 61

Figure 39. SEM images of $MgTiO_3$ ceramic (a) before HIPing, and (b) after HIPing. [13] 62
Figure 40. Relative density for the M0.95CT ceramics pressureless sintered at different temperatures. 63
Figure 41. Variation in Ɛr with frequency for the M0.95CT ceramic pressureless sintered at 1400 °C. 65
Figure 42. The average relative density and Ɛr (at 1 MHz) for the M0.95CT ceramics pressureless sintered at different temperatures. 66
Figure 43. Variation in Df with frequency for the M0.95CT ceramic pressureless sintered at 1400 °C. 67
Figure 44. The variation of resistivity with temperature for the M0.95CT ceramic pressureless sintered at 1400 °C. 68
Figure 45. Variation in Df with frequency for M0.95CT-HIP ceramic. 69
Figure 46. Variation in dielectric constant with frequency for M0.95CT and M0.95CT-HIP ceramics. 70
Figure 47. Resistivity of M0.95CT-HIP ceramic. 71
Figure 48. Hall-Effect and sheet carrier density for M0.95CT-HIP ceramic. 73
Figure 49. Absorbance with respect to wavelength for M0.95CT-HIP ceramic. ... 74
Figure 50. Determination of the Eg value of M0.95CT-HIP ceramic. 76

LIST OF ABBREVIATIONS

Å	Angstroms
au/arb units	Arbitrary units
σ	Conductivity
Df	Dielectric loss
Ɛr	Dielectric constant
ρ	Electrical resistivity
Eg	Energy band gap
GHz	Gigahertz
Hz	Hertz
Ɛr''	Imaginary part of permittivity
kHz	Kilohertz
MHz	Megahertz
m	Meter
µm	Micrometer
mm	Millimeter
nm	Nanometer
Qf	Quality factor
Ɛr'	Real part of permittivity
rpm	Round per minute
τf	Temperature coefficient of resonant frequency
wt%	Weight percent

CHAPTER 1

INTRODUCTION

Magnesium calcium titanate ($MgCaTiO_3$) dielectric ceramics take place an important position in fabrication of modern communication devices due to their good electrical properties such as quality factor (Qf), dielectric constant (Ɛr), and near-zero temperature coefficient of resonant frequency (τf). [1] The optimum combinations of these properties are required if they are to be used in special applications such as mobile phones, antennas, and global positioning systems.

Many microwave dielectric ceramics including $CaLaTi_4O_{15}$, $Ba(Y_{1/2}Ta_{1/2})O_3$, and $NdAlO_3$ exhibit good dielectric properties but, relatively high starting material cost and difficulties encountered in the preparation procedures restrict their usage. [2] $MgTiO_3$ ceramics not only have low material cost but also show good microwave properties including high Qf, and high Ɛr. However, its τf value, which symbolizes the change of the resonance frequency with temperature, is negative. [3] A large τf value imposes a limitation of $MgTiO_3$ ceramics for sensitive applications where the temperature change is high. For that reason, small amount of $CaTiO_3$ that has positive τf value is incorporated to$MgTiO_3$ ceramics to bring the τf value closer to zero. The $Mg0.95Ca0.05TiO_3$, (M0.95CT) composition meets the desired microwave dielectric properties with the high Qf (56.000 GHz), suitable Ɛr (20-21), and low τf (~0 ppm/ºC) values. [4]

Besides chemical composition, dielectric properties of ceramics are also highly dependent on microstructural features such as presence of second phase, grain size,

and porosity. [5] Therefore, in order to obtain desirable dielectric properties, appropriate synthesis and processing processes must be applied. M0.95CT ceramics could be produced by several methods such as the sol-gel, mixed oxide, high energy ball milling (HEBM) [6] coprecipitation, hydrothermal, and spray and freeze drying. [7] Among these methods, the mixed oxide method is commonly employed since it offers the advantages of large-scale production and low cost of processing.

The reagent-grade oxides MgO, TiO_2, and $CaCO_3$ in appropriate molar ratios are mixed and sintered to prepare M0.95CT ceramics by the mixed oxide method. [3] Undesirable $MgTi_2O_5$ phase often develops as an intermediate phase during sintering. Samyuktha et al. [8] concluded that removal of the secondary $MgTi_2O_5$ phase from samples using the mixed oxide approach is challenging because it demands a high sintering temperature of about 1450 ºC. Liou et al. [3] reported that as a result of solid-state sintering performed without calcination, M0.95CT ceramic contains a high amount (45.6%) of undesirable $MgTi_2O_5$ phase whose amount of this phase decreases to 37.2% as the sintering temperature increases. Although phase pure $MgTiO_3$ ceramics can be produced by the sol-gel and co-precipitation methods, these chemical processes are not efficient in terms of processing cost and time. [9]

High sintering temperatures lead to higher sintered density and consequently good dielectric properties but, the increase in grain size occurring during sintering should be avoided. Ferreira et al. [10] reported that the average grain size of the M0.95CT ceramics sintered at 1350 °C was 15.7 μm. As the temperature increased to 1400 °C, the grain size increased quickly to ~49.7 μm. Jawahar et al. [11] stated that abnormal grain growth and large grain sizes reduce the strength of ceramics. Compared to second phases and grain size, porosity has a more detrimental effect on the dielectric properties. The distribution, amount, and morphology of the pores adversely affect the mechanical performance of ceramic materials as well as their dielectric properties. [12] Microstructure with nearly full density and homogeneous

distribution of pores are required to achieve desirable dielectric properties. Sanoj et al. [6] confirm that liquid phase sintering provides full densification at lower sintering temperatures. However, it is well known that this sintering technique degrades the dielectric properties due to grain growth and the presence of the detrimental second phase at the grain boundaries.

Hot isostatic pressing (HIPing) is applied in an inert atmosphere to the pressureless sintered ceramic parts in order to eliminate or minimize the porosity present in the structure. An increase in density is reached as the pressureless sintered ceramic parts are HIPed since high pressures and temperatures could be applied simultaneously. The structural and physical properties of M0.95CT ceramics are expected to be improved by HIPing due to the reduction of the porosity since low partial oxygen pressure is practiced during sintering. [13]

The purpose of this research is to understand the effect(s) of HIPing on the microstructural development and dielectric properties of M0.95CT ceramics. The motivation was to get information and gain practice on the factors affecting the production of M0.95CT ceramics so that dielectric ceramics with better properties are produced domestically.

CHAPTER 2

LITERATURE REVIEW

2.1 $MgTiO_3$- $CaTiO_3$ Ceramics

$MgTiO_3$-based ceramics have been widely used as dielectric materials for resonators, filters, and antennas in communication systems such as radar and global positioning systems (GPS) that operate at microwave frequency. A well-known microwave material for dielectric resonators and filters is $MgTiO_3$-$CaTiO_3$. [14] The materials for microwave resonators and microwave device substrates must combine dielectric properties of a high dielectric constant (Ɛr), a low dielectric loss (Df) (high quality factor, where Qf = 1/tanδ), and a nearly zero temperature coefficient of resonant frequency (τf), in order to miniaturize the devices and for the systems to work with high efficiency and stability. [15]

$MgTiO_3$ has an ilmenite-type structure with following properties Ɛr = 17, Qf = 160,000 GHz, and Df = -50 ppm/°C. [16], [17] Ceramics made of a composition of 0.95$MgTiO_3$–0.05$CaTiO_3$ (M0.95CT) have Df = 0 with Ɛr = 21 and Qf = 56,000 GHz and meets the required dielectric properties with small amount of $CaTiO_3$ addition. [18]

The MgO-TiO_2 and CaO-TiO_2 binary phase diagrams are shown in Figure 1 and Figure 2, respectively. The stable phase mixture of $MgTiO_3$ and $MgTi_2O_5$ transforms to liquid phase between 1605 and 1660 °C, as represented in Figure 1. Liquidification temperature depends on the mixture ratios of $MgTiO_3$ and $MgTi_2O_5$ phases. The stable phase of $CaTiO_3$ transforms into liquid phase at 1970 °C, as seen in Figure 2. The TiO_2 content of the composition investigated in this study is very high compared to $CaTiO_3$, therefore 1460 °C is the minimum temperature for the development of

the liquid phase. Hence, 1460 °C was considered instead of 1970 °C for the determination of the maximum working temperature. Örek [19] also stated that during sintering process of the M0.95CT ceramic, 1460 °C is the maximum operating temperature for the synthesis as seen in the $MgTiO_3$- $CaTiO_3$ binary phase diagram in Figure 3. Therefore, during the calcination and sintering processes used to fabricate M0.95CT ceramics, operating temperatures above approximately 1460 °C should be avoided. Also, by selecting lower sintering temperatures, abnormal grain growth and occurrence of large grain size which lower strength and dielectric properties are hindered. [11]

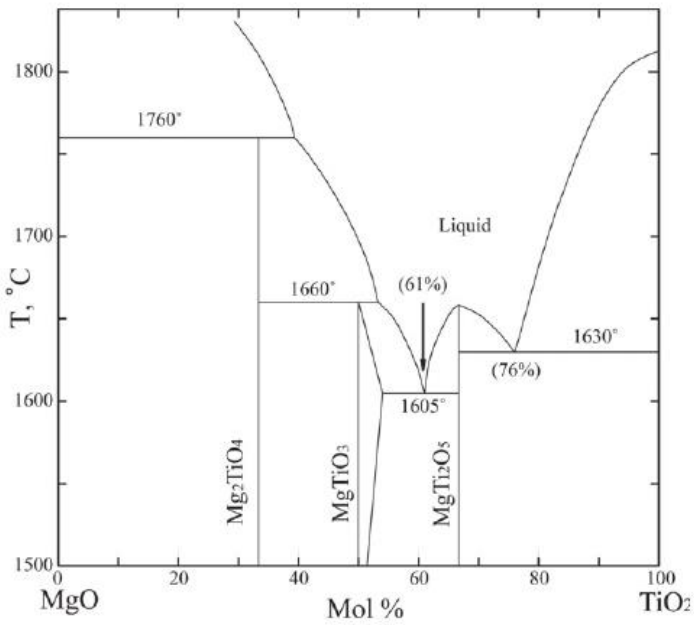

Figure 1. MgO-TiO_2 phase diagram. [20]

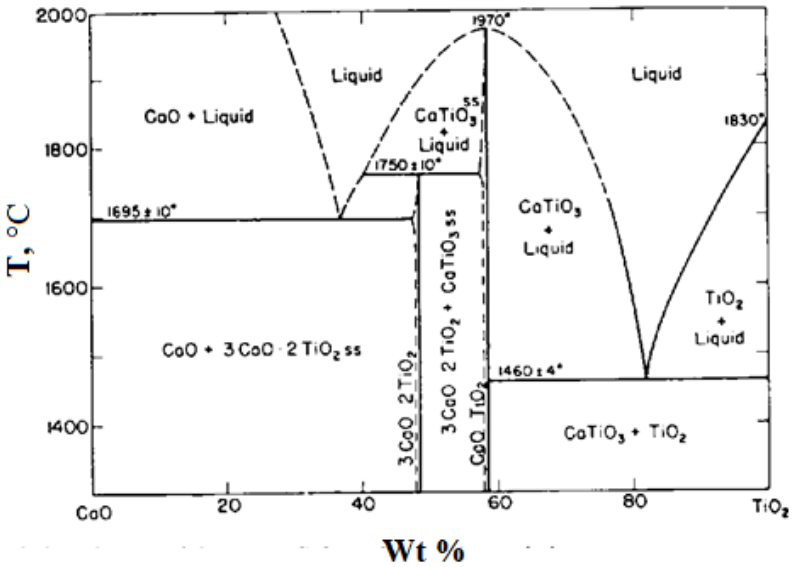

Figure 2. CaO-TiO_2 phase diagram. [21]

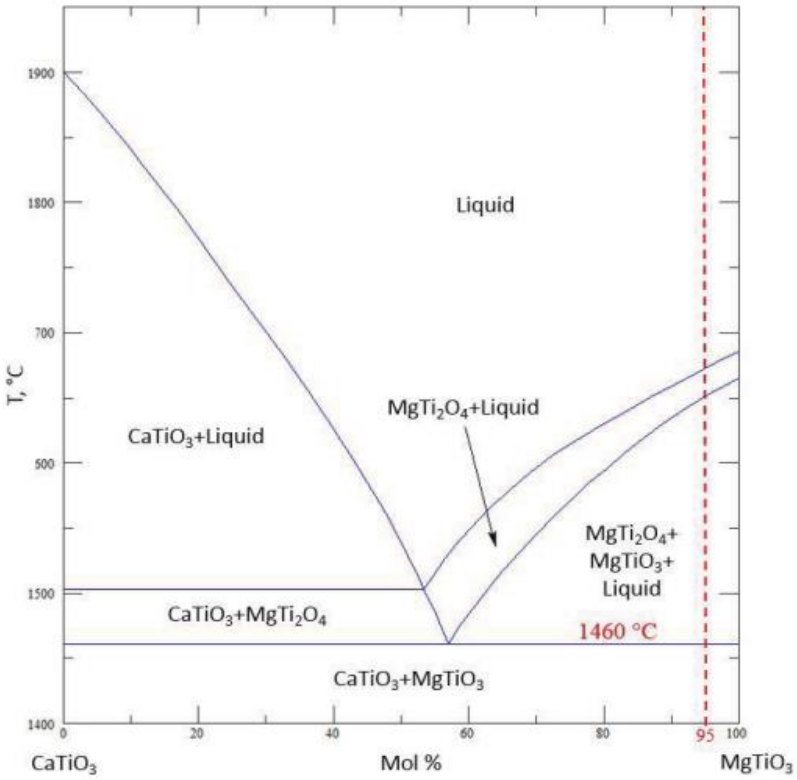

Figure 3. $MgTiO_3$- $CaTiO_3$ binary phase diagram. [19]

The effect of small quantities of dopants and glass additives on the sintering temperature and microwave dielectric properties of M0.95CT was investigated by several researchers. [22][23] Ichinose and Yamamoto [23] reported that the sintering temperature was reduced to approximately 1000 °C when 5 mol% V_2O_5 was added to M0.95CT powder. However, in this case the resultant sintered ceramic was multiphase, consisting of $MgTiO_3$, $MgTi_2O_5$, and $Ca_5Mg_4V_6O_{24}$ phases, and deterioration in the dielectric properties was recognized.

2.2 Dielectric Mechanisms

A dielectric material is an electrical insulator that may become polarized by an applied electric field in electromagnetism. [23] When an electric field is applied to a dielectric material, electric charges shift from their average equilibrium positions, leading to dielectric polarization. Dielectric polarization causes positive charges to move in the field's direction while negative charges move in the field's opposite direction. [24]

The four most common polarization mechanisms are atomic, ionic, dipole, and space charge polarization. Atomic polarization is the result of an external electric field being applied to the bulk material, which causes an electric strain to be produced in an atom. It happens when negatively charged electrons and positively charged nucleus of an atom move in the opposite direction of one another. It is schematically shown in Figure 4 (a). Ionic polarization results from the displacement of cations and anions in an ionic solid when it is exposed to an externally generated field. It is schematically shown in Figure 4 (b). The molecules are randomly orientated in the substance due to thermal activation in the absence of an electric field, and there is no net dipole moment. The external electric field attempts to align these asymmetric (polar) molecules with permanent dipoles parallel to the field when an alternating electric field is applied. This results in dipolar polarization, as seen in Figure 4 (c). Space charge polarization results from the accumulation of free charges at grain/ phase boundaries, defect regions, or free surfaces. Since the substance has an equal

quantity of positive and negative ions without an electric field, there is no separation of charges between the opposing ions. It is seen that the more mobile charges that are displaced by an external field and accumulate at barriers like grain/phase boundaries or at free surfaces with the application of an electric field. It is schematically shown in Figure 4 (d). [25]

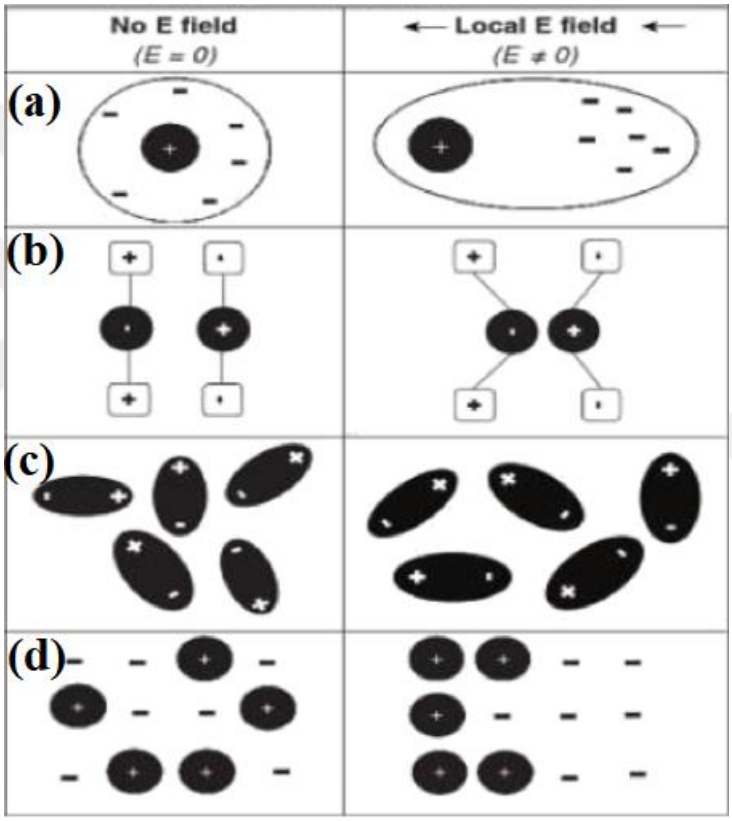

Figure 4. Schematics of (a) atomic, (b) ionic, (c) dipole, and (d) space charge polarization mechanisms. [25]

Electrical polarization is the most crucial characteristic of dielectrics, but their electrical conductivity is often low. Key characteristics of dielectrics in relation to semiconductors, a macroscopic description of electrical polarization, as well as various polarization mechanisms, are all taken into account. [26]

Total permittivity of a material is influenced by several polarization or dielectric processes, as displayed in Figure 5. Also, dielectric behavior can be influenced by a variety of dielectric mechanisms. At microwave frequencies, space charge and dipole orientation interact very significantly. Over the microwave area, ionic and atomic mechanisms are typically constant and rather weak. There is a characteristic "cutoff frequency" for each dielectric mechanism. The slower mechanisms gradually disappear as frequency rises, leaving the quicker ones to add to the real part of permittivity (Ɛr'). Each critical frequency corresponds to a peak in the imaginary part of permittivity (Ɛr'') in Figure 5. For various materials, each mechanism has a different magnitude and "cutoff frequency." [27]

The details of Ɛr' and Ɛr'' mechanisms are given in Section 2.3.

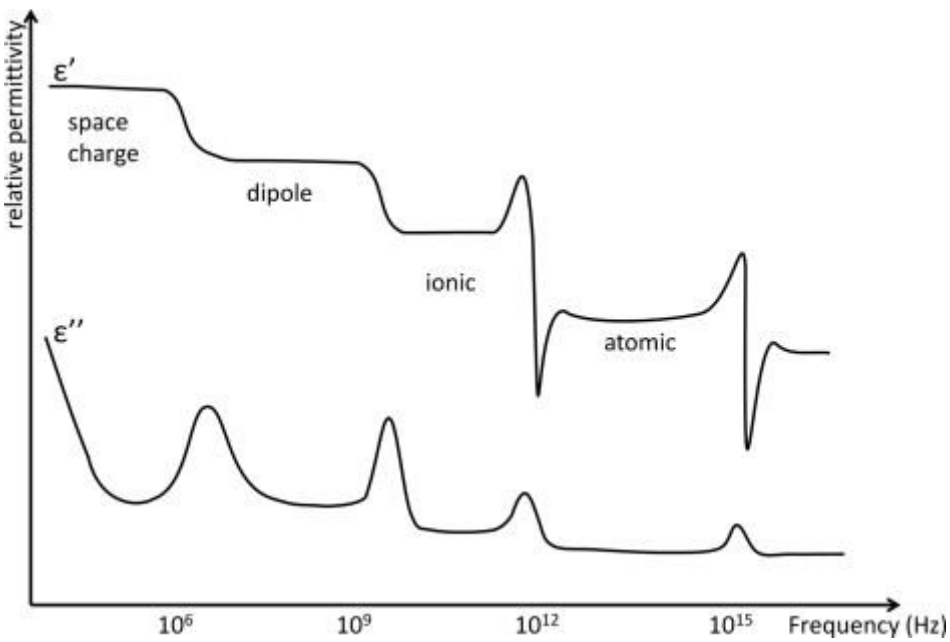

Figure 5. Variation of dielectric constant with frequency. [28]

2.3 Dielectric Constant and Loss

A substance is referred to as "dielectric" if it can store energy when an external electric field is introduced. [29] The dielectric constant and capacitance with a substance are related. If a parallel plate capacitor with a DC voltage source V is crossed as shown in Figure 6, more charge is stored when a dielectric substance is present between the plates than when nothing is there (a vacuum). [29]

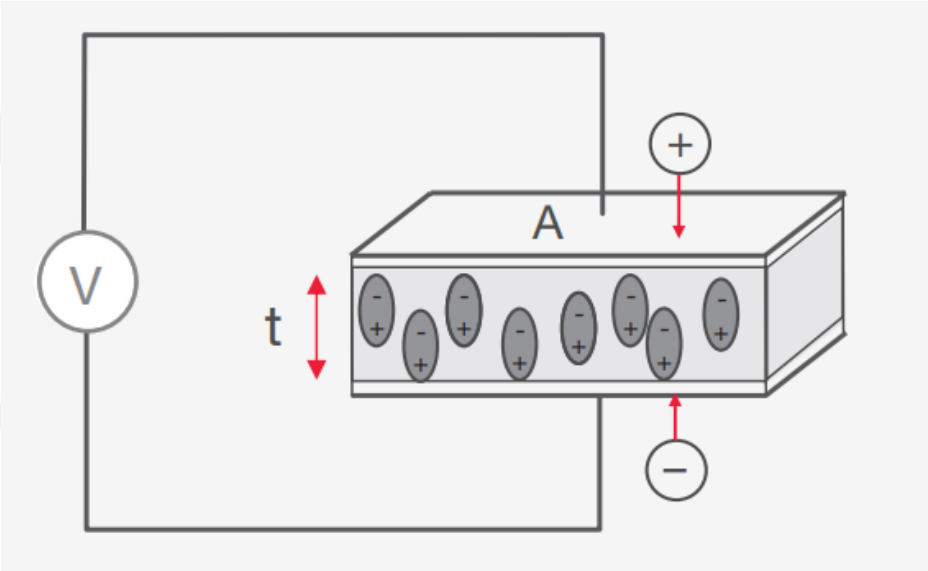

Figure 6. Parallel plate capacitor schema (DC case). [27]

According to Eqns (1) and (2), capacitance and dielectric constant of the dielectric materials are connected. A and t are the area of the capacitor plates and their distance from one another, respectively, while C and C_0 represent capacitance with and without a dielectric, respectively, as shown in Eq (2).

$$C_0 = \frac{A}{t} \qquad \text{Eq. (1)}$$

$$\varepsilon r = C / C_0 \qquad \text{Eq. (2)}$$

The amount of energy from an external electric field that is stored in a material is indicated by the real part of permittivity (Ɛr'). Loss factor (Df), often known as the imaginary part of permittivity, is a measurement of how dissipative or lossy a material is to an external electric field. The imaginary part of permittivity (Ɛr ") is often significantly less than Ɛr' and is always larger than zero. Both conductivity and dielectric loss are factors in the loss factor. [27]

The real and imaginary components are 90° out of phase in a basic vector diagram of complex permittivity as shown in Figure 7. The ratio of the Ɛr " to the Ɛr' is known as the loss tangent, or tanδ. The Q stands for quality factor, while Df stands for dissipation factor. The Df and tanδ are the same for the loss tangent, as indicated in Eq (3). The reciprocal of Df, an electronic microwave material, is also referred to as Q. [27]

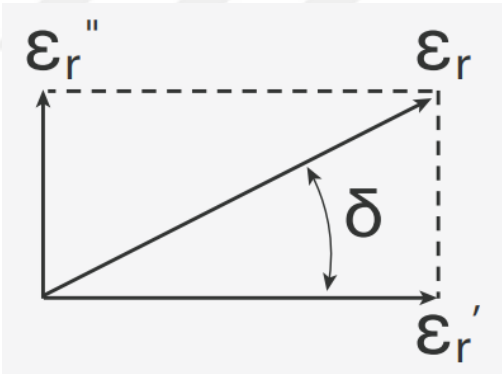

Figure 7. Loss tangent vector schema. [27]

$$\tan\delta = \frac{\varepsilon r''}{\varepsilon r'} = Df = \frac{1}{Q} \qquad \text{Eq. (3)}$$

2.4 Mixed Oxide Method

Mixed oxide method is commonly used for the production of ceramic parts in perovskite structure, ABO_3, where A is an alkaline earth metal and B is a transition metal (B ≡ Ti, Zr, Mn, Fe, or Co). The mixed oxide method is a very suitable method for large-scale production and low cost of processing. It is commonly used to fabricate capacitors, transducers, non-volatile ferroelectric memory devices, high temperature piezoelectric sensors [30], and dielectric substrates etc. It has the disadvantages of low homogeneity and purity. [7] The parameters affecting the processing in the mixed oxide method are particle system, particle characteristics, mixing time, compaction technique and pressure, sintering type and conditions (time, temperature, pressure, etc.). [31]

In order to fabricate ceramic parts by the mixed oxide method, multicomponent oxide powders, starting ingredients, often metal oxides and carbonates are first blended together. Then, the resulting mixtures are crushed or milled followed by compaction. After compaction, a calcination procedure is applied several times with intermediate grinding steps. The grinding process may introduce contaminants into the system. It also produces particles with angular shapes. [32]

Compaction of the powder comes after the calcined and ground powder has been combined with processing additives. External pressure may be applied to get greater compact densities. Usually, uniaxial die pressing is applied for compaction. As compaction occurs, the number of contact points between the particles increases. The form and size of the particles can have an impact on compaction behavior. [33]

Following the compaction step, the compacts are pressureless sintered at elevated temperatures usually in air. As necessary throughout the sintering process, the powder particles do not melt; rather, atomic diffusion takes place in the solid state to bring the particles together and reduce the porosity (i.e., densification) of the body. Although the simplest kind of sintering is solid state sintering, the processes that take place and how the particles interact may be rather complicated. Reduced surface free

energy of the consolidated mass of particles is the driving force for sintering. Atom diffusion mechanisms that either densify the body (by moving materials from inside the grains into the pores) or coarsen the microstructure can achieve the reduction in the surface free energy. In coarsening, the rearrangement of matter between different parts of the pore surfaces takes place without actually leading to a decrease in the pore volume. The coarsening process decreases the driving force for power for densification. This interaction is frequently described as a conflict between densification and coarsening during the sintering process. [29]

The flowchart showing the main steps involved in the production of polycrystalline ceramics by the mixed oxide method is presented in Figure 8.

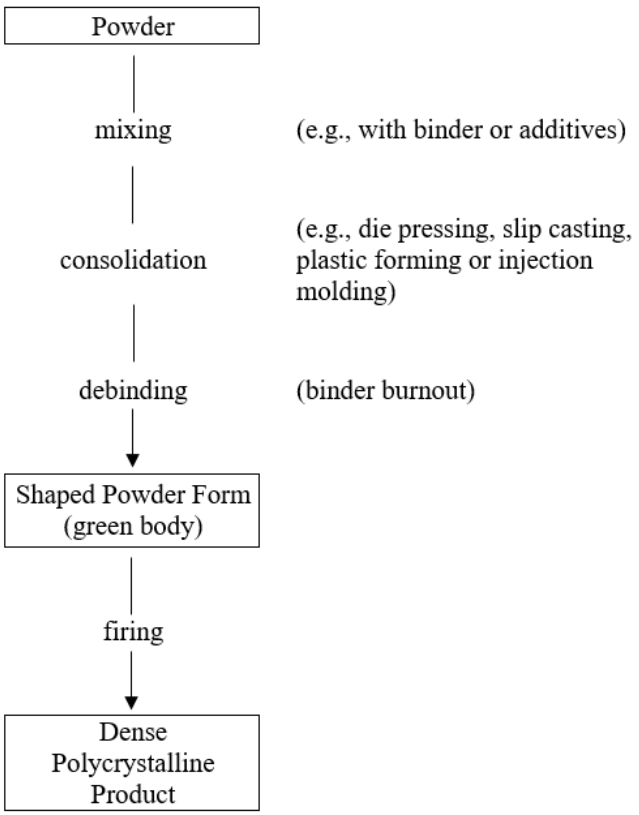

Figure 8. Flow chart showing the main steps involved in the production of polycrystalline ceramics. [29]

2.5 Hot Isostatic Pressing (HIPing)

Hot isostatic pressing (HIPing) provides consolidation of workpiece (usually powder) by using isostatic pressure and heat simultaneously. The HIP process uses argon or nitrogen as inert gas to apply high pressure (50-200 MPa) and high temperature (300-2500 °C) to the exterior surface of workpiece. [34]

The workpiece is generally enclosed in an evacuated glass, ceramic, or sheet metal capsule. In order to prevent deformation during compression, care must be given throughout the capsule's design and filling process. Encapsulation is not necessary for sintered or casted workpiece since the surface of the workpiece acts as its own capsule. [35] There are two main routes for HIPing ceramics, as shown in

Figure 9.

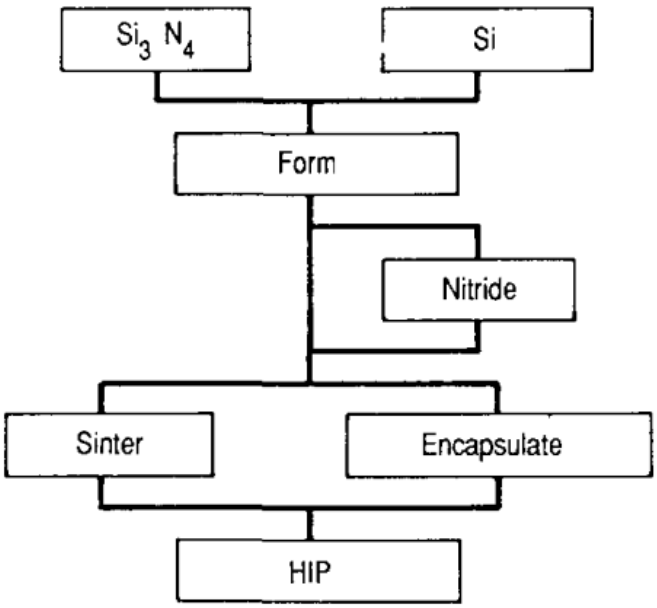

Figure 9. HIPing of Si_3N_4 ceramics. [35]

In the first technique, the desired shape is created by cold isostatic pressing with machining, injection molding, extrusion, or slip casting using ceramic powder with additives. Precision and repeatability of the density distribution are required in order to obtain excellent tolerances in the finished product. Before encapsulation, forming ingredients like plasticizers and binders are taken out of the green body. A cover of glass is then placed to the body. The glass is sealed using hot evacuation, which can be done in a vacuum furnace before being heated up and transferred to a HIP unit. After cooling, the glass capsule is fractured, and the piece is removed using sandblasting. The benefit of this process is that it requires a negligible quantity of sintering aids, whereas other procedures typically do not allow for good densification. Low enclosing temperatures help to prevent weight loss and decomposition.

Encapsulation is not used in the second technique. After the green body is formed, the body is sintered to eliminate interconnected pores. Next, the green body is HIPed. This technique frequently causes significant weight loss that affects composition and tolerances. With some effectiveness, nitrogen gas has been utilized to prevent breakdown in silicon nitride, and oxide ceramics have also benefited from the application of oxygen partial pressures. The cost of encapsulation is reduced with this technique. [35]

HIP was initially used with pressure bond or diffusion bond fuel components. However, its promise in other unconnected fields was immediately realized. Soon after its discovery, it was applied to the significant areas; removing internal casting flaws and restoring the functionality of castings that have been harmed by service, diffusion bonding, sintering and densification of ceramics, and powder metallurgy. [35] Alumina, silicon carbide, silicon nitride, lead zirconate-titanate, yttria stabilized zirconia, and other ceramics have all been produced by HIPing.

2.6 Resistivity

Electrical resistivity (ρ), which measures a substance's resistance to current flow and is the inverse of conductivity (σ), is a fundamental attribute of materials. [36] Resistivity is one of the most sensitive measures of the electrical transport in materials. It ranges from 10^{12} cm for the best insulators to 10^{-6} cm for a typical metal. Conductivity in semiconductors is determined by the availability of charge carriers (electrons or holes) and the mobility of the carriers. [37] Conductivity has many processes which affects how it responds to temperature. Because more carriers are produced as temperature rises in semiconductors, conductivity increases but, in metals, conductivity decreases as temperature rises (more scattering by the lattice). [38]

Whether a thin film or a bulk sample of the material is being used to measure conductivity will affect the method employed to do so. While just somewhat more challenging, a four-point bulk measurement provides substantially higher accuracy. The four-point probe approach, as shown in Figure 10, uses four equally spaced in-line probes with modest probe tip sizes compared to the probe spacing. The probe tip and the sample are considered to have ohmic contact. The voltage difference is measured between the two inner probes, while current is typically transmitted between the two outside probes. [37]

In a four-point probe measurement, resistivity is calculated by Eq (4)

$$\rho = 2\pi sFV/I \qquad \text{Eq. (4)}$$

if a correction factor (F), measured voltage (V), force current (I), and probe spacing (s) are used. When placing probes close to the center of a material with a semi-infinite thickness and a bigger area, the probe spacing, F, is unity. [37]

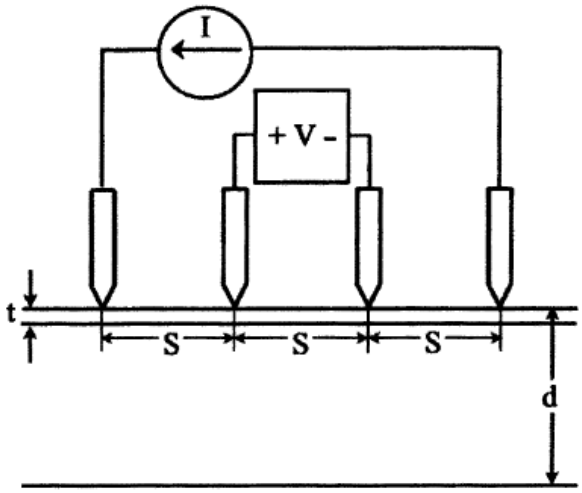

Figure 10. The four-point probe approach schema. [37]

2.7 Hall Effect

The ratio between the induced electric field and the sum of the applied magnetic field and current density is known as the Hall coefficient. Hall effect measurement schema is shown in Figure 11. Due to the fact that its value is influenced by the type, number, and properties of the charge carriers that make up the current, it is a property of the material from which the conductor is produced. [39] The Hall effect is a modular approach that provides data on carrier concentrations, mobility, and indirectly estimates of scattering processes, all of which alter conductivity as a function of temperature. [37]

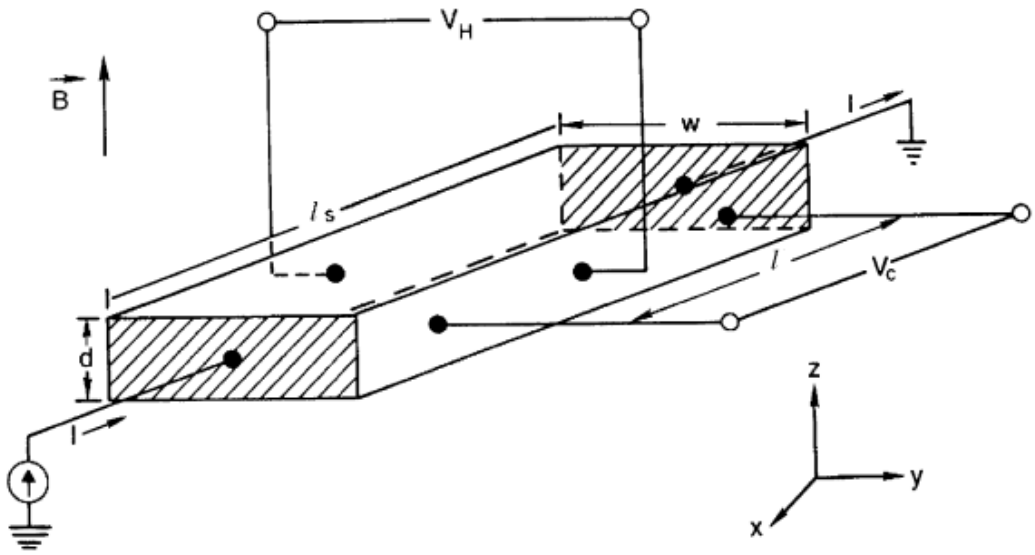

Figure 11. Hall-Effect Measurement Schema. [37]

Numerous criteria, such as available size, manufacturing methods, measurement time constraints, etc., should be taken into account when choosing the type of geometrical structure to utilize for a particular application. Figure 12 illustrates six of the most common structures in consideration of these factors. Almost every semiconductor material responds favorably to indium when applied with a soldering iron. Considering the geometry of the sample produced and the ease of applying indium, in this study, the square configuration was used in the Hall effect measurement. [37]

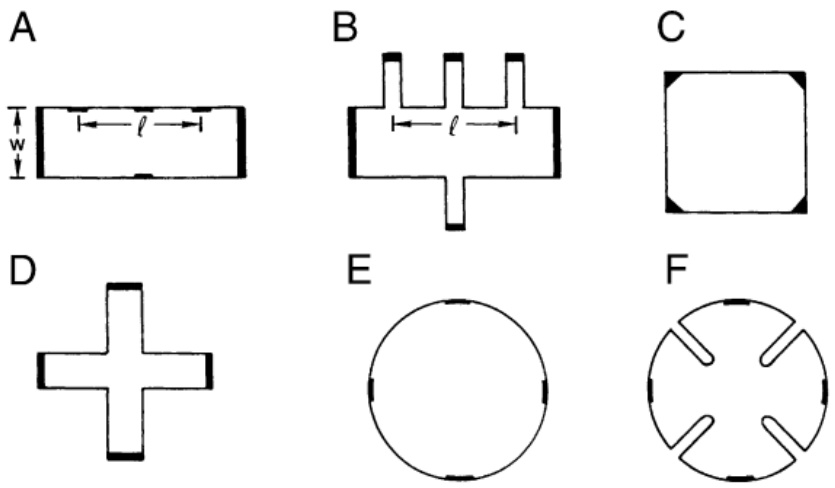

Figure 12. Different configurations for Hall effect measurements: (A) Hall bar; (B) Hall bar with contact arms; (C) Square; (D) Greek cross, (E) Circle; (F) Cloverleaf. [37]

2.8 Absorbance

The measurement of a light beam's attenuation after it has passed through a sample or has been reflected off a sample surface is known as ultraviolet (UV) and visible (UV-Vis) absorption spectroscopy. [37] Molecules often experience electronic excitations in the UV and visible spectrums. From the UV to the near infrared (NIR), charge transfer bands are possible. The band gap of a semiconductor can range from the UV to NIR and is dependent on the material and physical parameters. The process of preparing samples for UV-Vis spectroscopy is often simple. A suitable solvent or pH buffer is used to detect absorbing chemical composition that are in solution or that can dissolve. [37]

Since UV-vis spectroscopy examines electrical transitions between the valence band (VB) and the conduction band (CB), it provides a practical approach for determining the optical band gap for semiconductors. The energy difference between the valence band minimum (VBM) and the conduction band maximum (CBM), which is the

definition of the electronic band gap, is not always equal to the optical band gap; however, it is frequently approximated as such because there are few practical ways to measure the electronic band gap. [40]

An electron needs a specified minimum amount of energy for the transition, known as the band gap energy, in order to go from a VB to a CB. The semiconductor industries both depend on accurate band gap measurements. In comparison to semiconductors, insulators have a higher band gap energy (i.e., > 3 eV). [41]

$$E = \frac{hc}{\lambda} \qquad \text{Eq. (5)}$$

where; h is 6.626×10^{-34} JS, and c is 3×10^{8} ms^{-1}.

CHAPTER 3

EXPERIMENTAL PROCEDURE

3.1 Sample Preparation

M0.95CT ceramics were prepared by the mixed oxide method. Reagent grade Magnesium oxide (MgO), Calcium carbonate ($CaCO_3$), and Titanium dioxide (TiO_2) powders used in this study were supplied from local companies. Name, chemical formula, supplier, and purity of the powders used in the production of M0.95CT ceramic are listed in Table 1. Particle size of the starting powders varied in the range of 1-10 µm according to Certificate of Conformance (COC) document.

Table 1. Powders used in the production of M0.95CT ceramics.

Powder Name	**Chemical Formula**	**Supplier**	**CAS No.**	**Purity (wt%)**
Calcium Carbonate	$CaCO_3$	Acros Organics	471-34-1	99
Magnesium Oxide	MgO	Kümaş	1309-48-4	98.8
Titanium Dioxide	TiO_2	Aklar Kimya	13463-67-7	99

First the starting powders were weighed using a precision balance (OHAUS pionner) with high accurracy (±0.0001) to their predetermined amounts. Then, the powders were wet mixed in a ball mill at 60 rpm using distilled water. Alumina balls and alumina jar were used as milling medium. The mixed powders were dried in a drying oven at 120 °C for 24 h. The dried powder mixture was compacted using single action pressing. Pressing was carried out in a tool steel die at 10 mm/s pressing speed

up to a pressure of 45 MPa without binder addition. Square shaped pelets with smooth curves at the corners had nominal dimensions of 50 mm length and 6 mm thickness. The pellets were calcined in air at 1050 °C for 3 h. During calcination, a heating and cooling rate of 4 °C/min was arranged. Schematic of calcination was represented in Figure 13.

Figure 13. Calcination schedule.

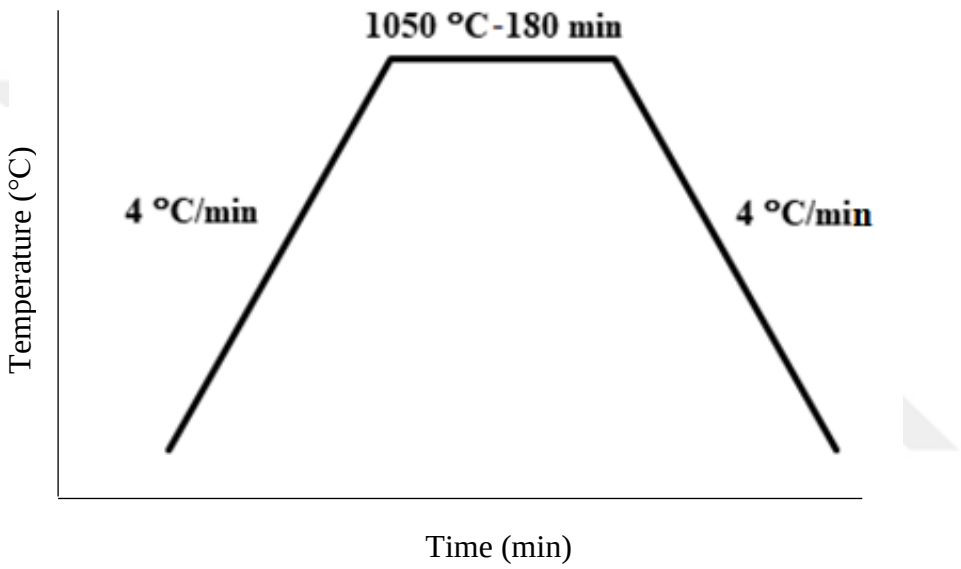

The calcined powder in chunk form was crushed and ground by mortar with pestle. In order to obtain a homogeneous mixture, the grinding process was performed further in a ball mill using an alumina jar with alumina balls at 60 rpm for 24 h. Distilled water was used for milling medium. After ball milling, the slurry obtained was dried in an oven at 120 °C for 24 h. A second calcination process having the same calcination schedule with the first one was performed at 1050 °C for 3 h to ensure that all the starting powders have reacted and the desired phases have been obtained.

The comminution processes performed after the first calcination were repeated also after the second calcination and M0.95CT powder was obtained. After that,

M0.95CT powder was mixed with only distilled water without any binder addition and dried in the same way previously done after the first calcination. Dried M0.95CT powder was combined with 0.5 wt% polyvinyl alcohol (PVA) in an agate mortar with pastle and sieved through a 60 μm screen to produce a fine, homogenous powder for pressing. In order to get a compact with the required size and geometry, compaction of the powder was accomplished by uniaxial pressing in a tool steel die at various (80, 120, 160, 200, and 240 MPa) pressures.

Square shaped compacts with smooth curves at the corners having nominal dimensions of 40 mm in size and 5 mm in thickness were pressureless sintered in air at temperatures of 1300, 1350, and 1400 °C. Sintering took place in three steps as shown in Figure 14. In order to eliminate organic residuals introduced from ball milling process and binder addition, green bodies were first heated to 600 °C at a rate of 4 °C/min and soaked there for 30 min. In order to be sure that there is no unreacted powders, the temperature was brought to the calcination temperature for 1 h. The temperature was then increased for the same durations (1 h) to the maximum sintering temperature at 1300, 1350, and 1400 °C. The heating and cooling rates were 4 °C/min. Figure 15 (a) shows a pressureless sintered M0.95CT ceramic pellet.

The pressureless sintered pellets were then HIPed at 1200 °C at 120 MPa for 1 h. Hereafter the M0.95CT ceramic first pressureless sintered at 1400 °C and then HIPed at 1200 °C will be called M0.95CT-HIP ceramic. During HIPing, Argone (Ar) gas was used as the inert atmosphere. Gas flow continued throughout the HIPing. Figure 15 (b) shows a M0.95CT-HIP ceramic pellet. It can be interpreted that there is a noticiable color change after HIPing, and dark-coloered pellet was obtained.A 10 °C/min of heating and cooling rate was applied during HIPing. The HIPing schedule displaying the time, temperature, and heating rate for the preparation of the M0.95CT-HIP ceramic was illustrated in Figure 16.

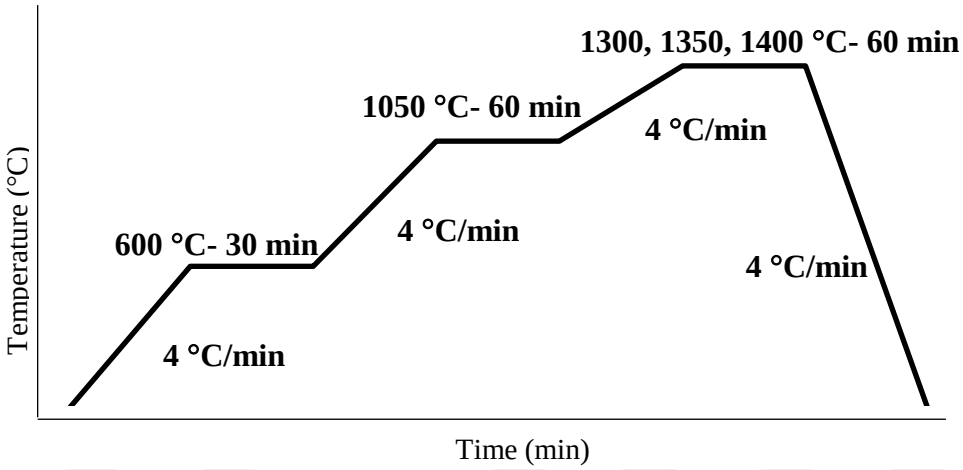

Figure 14. Sintering schedule for M0.95CT ceramic.

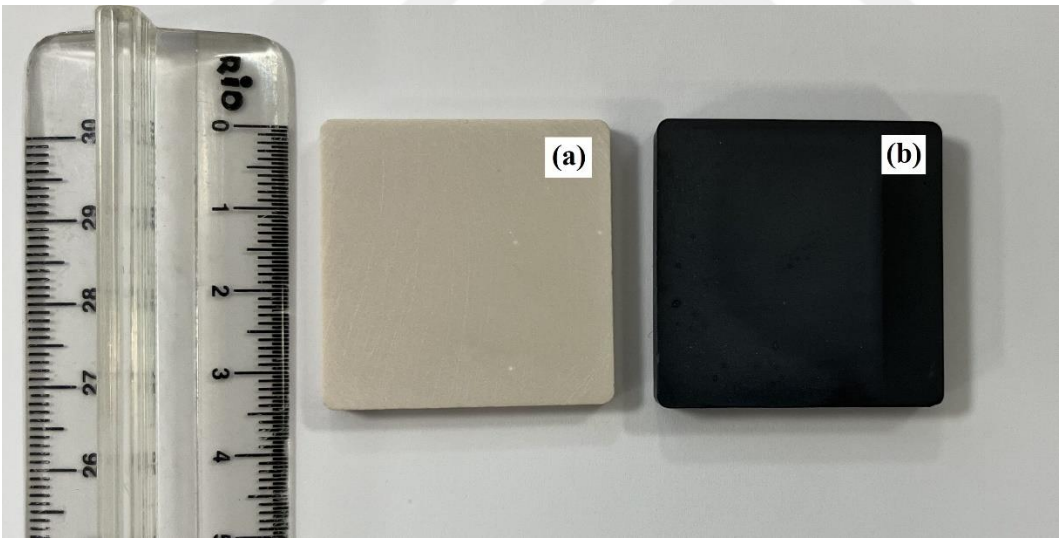

Figure 15. M0.95CT ceramic pellets; (a) pressureless sintered at 1400 °C, and (b) HIPed at 1200 °C.

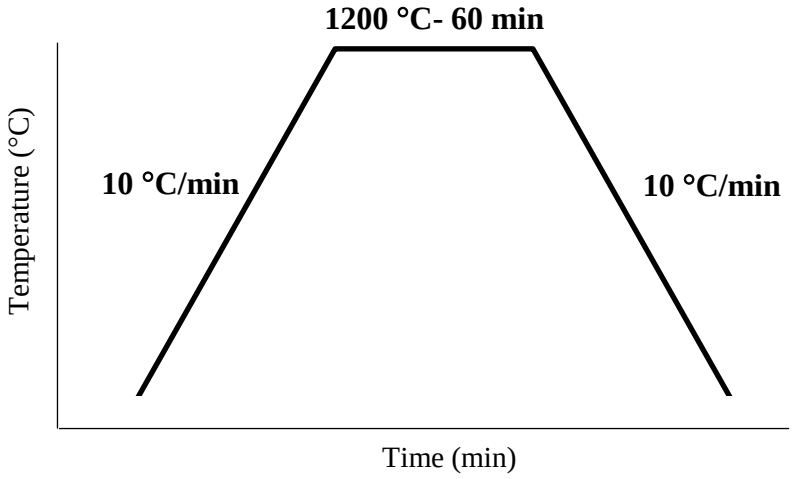

Figure 16. HIPing schedule for M0.95CT-HIP ceramic.

The process flow diagram including the steps used in the production of M0.95CT and M0.95CT-HIP ceramics is shown in Figure 17.

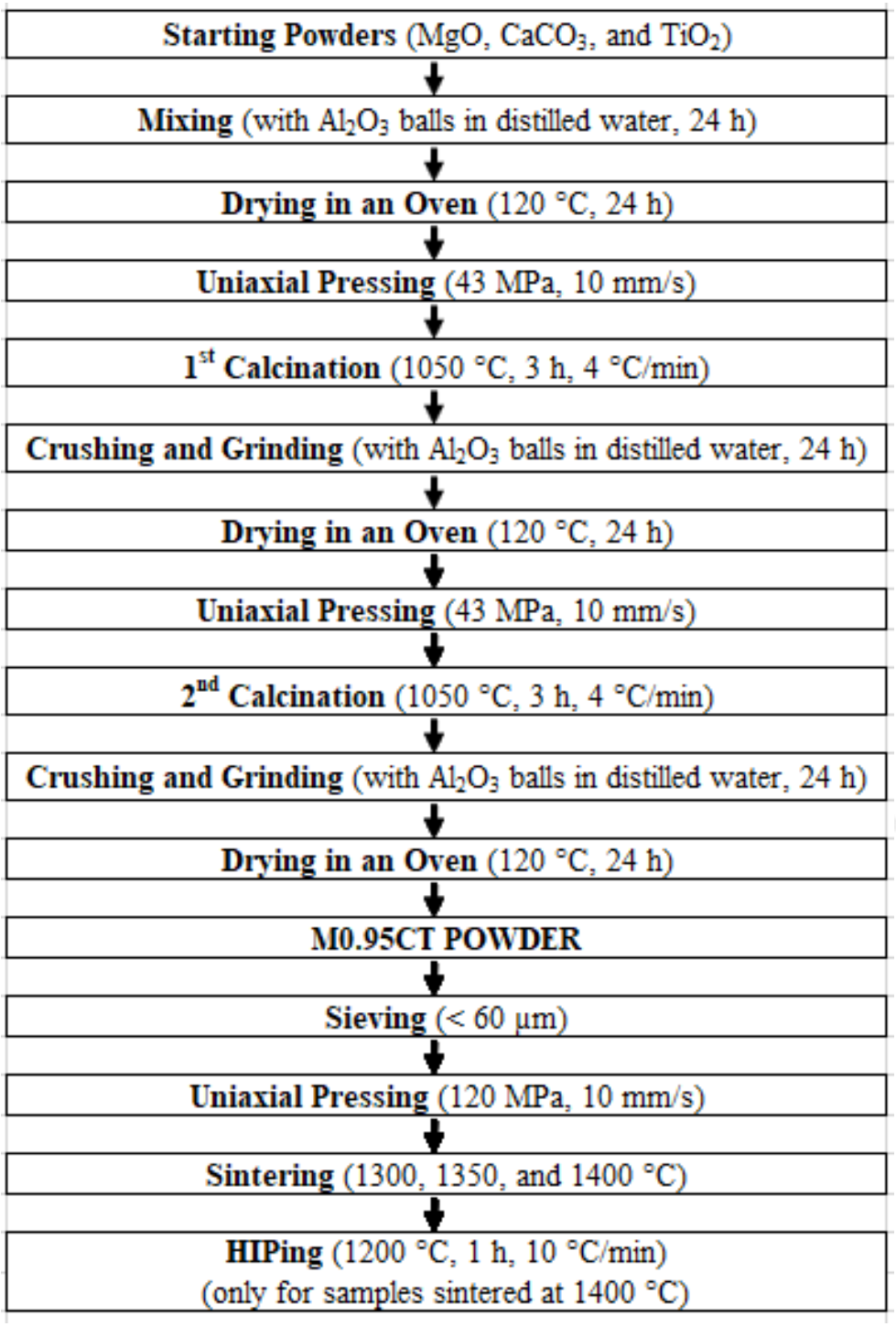

Figure 17. The process flow diagram including the steps used in the production of M0.95CT and M0.95CT-HIP ceramics.

3.2 Characterization

3.2.1 X-Ray Diffraction (XRD) Analysis

An X-Ray diffraction analyzer (XRD, Rigaku Miniflex 600) was employed to identify the crystal structure and the phases present in the starting, calcined, and M0.95CT powders as well as the pressureless sintered M0.95CT ceramics and M0.95CT-HIP ceramics. X-Ray analyses were done using Cu-Kα radiation (λ = 1.5418 Å) between 2θ of 10 and 90° at a voltage of 40 kV at a scan rate of 2 °/min. XRD patterns were investigated by PDXL (Integrated X-Ray Powder Diffraction Software).

3.2.2 Scanning Electron Microscopy (SEM) Analysis

A Scanning Electron Microscopy (SEM, Zeiss Merlin/Feg) was used to examine the microstructure of M0.95CT and M0.95CT-HIP ceramics. Fracture surface, polished and chemically or thermally etched surface of both ceramics were examined using SEM. Back-scattered imaging was done for distribution of the phases in the structure since it creates contrast difference. The operational voltage varied from 5 to 20 kV. Before SEM examination, all ceramics were sputter coated with a thin layer of gold to provide conductivity.

3.2.3 Energy Dispersive Spectroscopy (EDS) Analysis

An Energy Dispersive Spectroscopy (EDS), attached to SEM was used to examine compositional variations in M0.95CT and M0.95CT-HIP ceramics. The operational voltage was 20 kV.

3.2.4 Particle Size Analysis

Particle size analyzer (Malvern Mastersizer 2000 Ver. 5.40) was used to measure particle size and size distribution of the particles in the starting powders and in the calcined M0.95CT powder. Distilled water was used as dispersion medium. Each measurement was repeated 3 times and the mean average was taken as data.

3.3 Property Measurement

3.3.1 Density

The density and open/closed pore ratio of M0.95CT and M0.95CT-HIP ceramics were calculated in accordance with the Archimedes' technique. A precision digital balance (Sartorius CP224S) was employed for measurements. Xylene with a density of 0.865 g/cm^3 [42] was used for the measurements since it can penetrate the pores in the sample more effectively. With the use of metal hanger, the sample to be evaluated was immersed in xylene for 24 h, and the balance was measured. Density value was calculated using Eq (6).

$$\rho(ceramic) = \frac{m(air) \times \rho(xylene)}{m(xylene-air) - m(xylene)} \qquad \text{Eq. (6)}$$

Where;

- $\rho_{ceramic}$: The calculated density of the ceramic (g/cm^3)
- m_{air}: The weight of the ceramic measured in air (g)
- m_{xylene}: The weight of the ceramic measured in xylene (g)
- $m_{xylene\text{-}air}$: The weight of the ceramic removed from the xylene by quickly drying the outside (g)
- ρ_{xylene}: The density of xylene (g/cm^3)

In order to manage the production of a high quality ceramic item with regard to its ultimate size and shape, the porosity, and microcracks in the body knowing the compact density of a green ceramic body is essential. Archimedes' method is not suitable for the determination of the density of green body ceramics due to dispersion of the body in the solvent. [43] A micrometer was employed to measure the nominal dimensions hence, to calculate the density of the green body of M0.95CT ceramics.

3.3.2 Dielectric Constant and Dielectric Loss

The ε_r of the M0.95CT ceramics pressureless sintered at temperatures of 1300, 1350, and 1400 °C, and HIPed at 1200 °C was measured in accordance with parallel plate (electrode) capacitor technique using an LCR (Inductance Capacitance Resistance) meter, (Hioki IM3536). Also, Df of the M0.95CT ceramic pressureless sintered at 1400 °C was measured before and after the application of HIPing using the same technique that operates at low frequencies (less than 1 GHz). [44] The ε_r values at the microwave frequency range (1-3 GHz) [45] could not be measured with this device. Parallel plate test parameters are obtained by considering the dimensions of the material and measuring the capacitance (C) and Df. The measurement of the ε_r uses the C value. This technique has simple sample preparation and setup requirements and high measurement accuracy (± 1% for ε_r and 5% ± 0.005 for Df). However, if air gap and its effects are not considered and calibrated, they might lead to considerable errors. Additionally, the electrode polarization effect might lead to inaccurate results. High frequency measurement provides more accurate outcomes since this affect decreases with increasing frequency. [44] Measurement frequency was kept at 1 MHz for this study. Also, alumina (Al_2O_3) ceramic with 4 mm thickness as a reference sample was used to ensure measurement accuracy.

Before the measurements, surfaces of the pellets were ground and polished to obtain flat and parallel surfaces. The surfaces of the pellets with 35 mm in length were first

roughly ground using SiC sandpapers to get the reference sample thickness of 4 mm. Then, lapping was applied to achieve a polished and parallel surface. In order to evaporate the lapping liquid accumulated in the pores of the pellets, the pellets were placed in a drying oven and dried at 120 °C for 1 h. The measurement was carried out by clamping the pellet between two parallel electrodes with 29.73 mm diameter. Therefore, there was no need for the metallization of the pellet.

By using fixed electrodes rather than metallization, the cost of the paste (gold or silver) can be reduced and the heat treatment needed for the paste's drying can be avoided.

3.3.3 Resistivity

The resistivity of the M0.95CT ceramics pressureless sintered at 1400 °C were measured before and after the application of HIPing in accordance with four-probe method using an electric resistance measurement instrument (Advance Riko, ZEM-3 Series). The measurements were performed from room temperature up to 400 °C at 100 °C intervals. The calibration of the device was tested using constantan alloy (55% copper and 45% nickel alloy).

After going through the surface preparation procedure (lapping and polishing) as explained in Section 3.3.2, the pellets were brought to nominal dimensions of 4 mm square and 10 mm length for the measurement.

3.3.4 Hall Effect

The majority carriers (electrons or holes) of the M0.95CT ceramics pressureless sintered at 1400 °C were measured before and after the application of HIPing using Hall effect measurement instrument (Lakeshore 7600 Series). The measurements were performed at room temperature. After going through the surface preparation procedure (lapping and polishing) as explained in Section 3.3.2, the pellets were

brought to nominal dimensions of 20 mm square and 2 mm thickness for the measurement. Square geometry, shown in Figure 12 (c), was selected for measurement. Then, indium contacts with a dimension of 1 mm or less were placed on the corners.

3.3.5 Absorbance

The energy band gap (Eg) of the M0.95CT ceramics pressureless sintered at 1400 °C were measured before and after the application of HIPing using UV-Vis Spectrometer (Scinco). The measurements were performed at room temperature. Sintered ceramic was crushed in a mortar with a pestle to micrometer size of particles. Approximately 100-150 mg powder was mixed with ethyl alcohol for the measurement.

CHAPTER 4

RESULTS AND DISCUSSION

4.1 Characterization of Starting Powders

4.1.1 Particle Size Analysis

Particle size distribution histogram of the MgO starting powder is shown in Figure 18. Particle size analysis revealed that the powder has three modal distribution. The size of the particles ranges from 0.6 to 36 µm. The average particle size, d_{50}, is 5.642 µm. The values of d_{10} and d_{90} are 1.148 and 18.636 µm, respectively. The supplier of the powder reports that the particles in the powder are in the range of 1-10 µm and the average particle size is approximately 5 µm. The particle size data reported by the supplier was confirmed by particle size measurement of the MgO starting powder.

Figure 18. Particle size distribution histogram of the MgO starting powder.

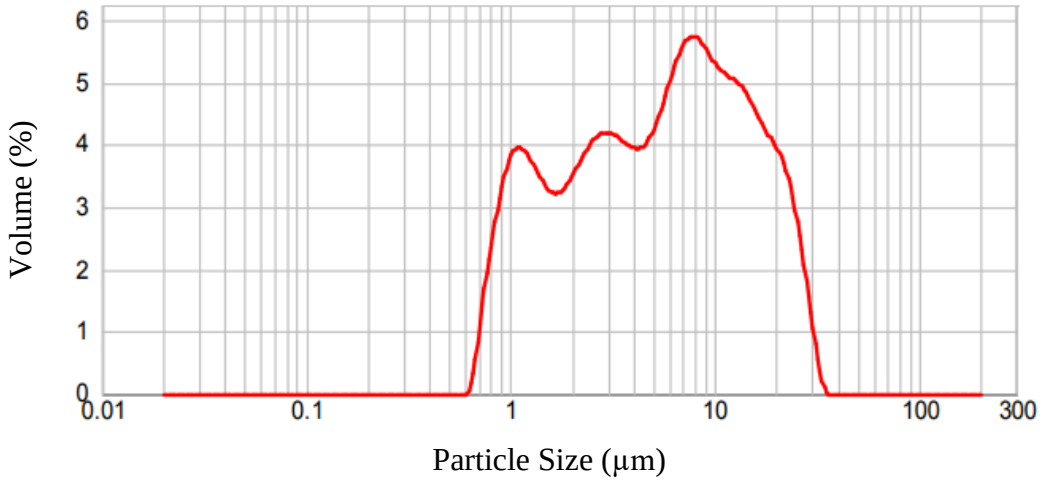

Particle size distribution histogram of the $CaCO_3$ starting powder is shown in Figure 19. Particle size analysis showed that the powder has multimodal distribution. The

size of the particles ranges from 0.16 to 20 µm. The average particle size, d_{50}, is 1.725 µm. The values of d_{10} and d_{90} are 0.283 and 8.286 µm, respectively. The supplier of the powder reports that the particles in the powder are in the range of 1-10 µm. The particle size data reported by the supplier was confirmed by particle size measurement of the $CaCO_3$ starting powder.

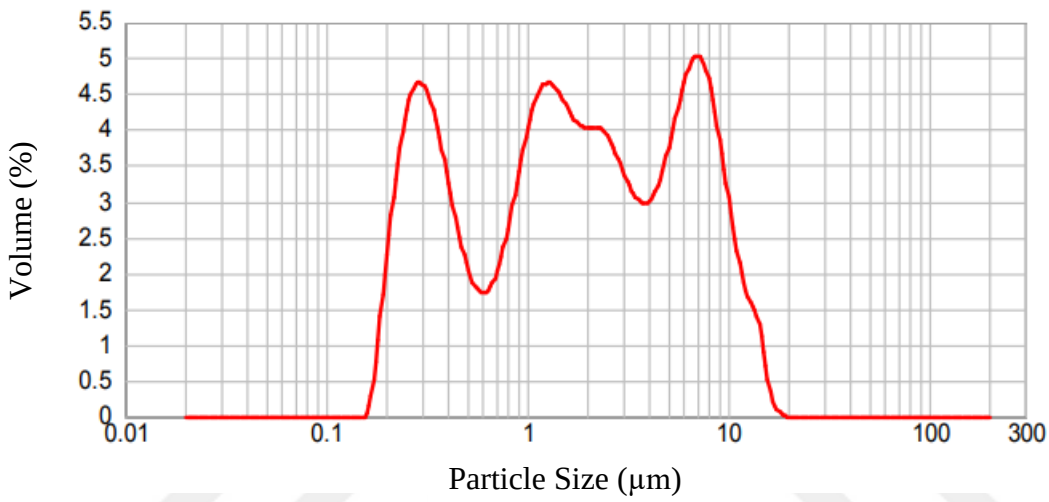

Figure 19. Particle size distribution histogram of the $CaCO_3$ starting powder.

Particle size distribution histogram of the TiO_2 starting powder is shown in Figure 20. Particle size analysis revealed that the powder has unimodal distribution. The size of the particles ranges from 0.03 to 2 µm. The average particle size, d_{50}, is 0.451 µm. The values of d_{10} and d_{90} are 0.127 and 1.110 µm, respectively. The supplier of the powder reports that the average particle size is approximately 5 µm. The particle size data reported by the supplier was higher than particle size measurement of the TiO_2 starting powder.

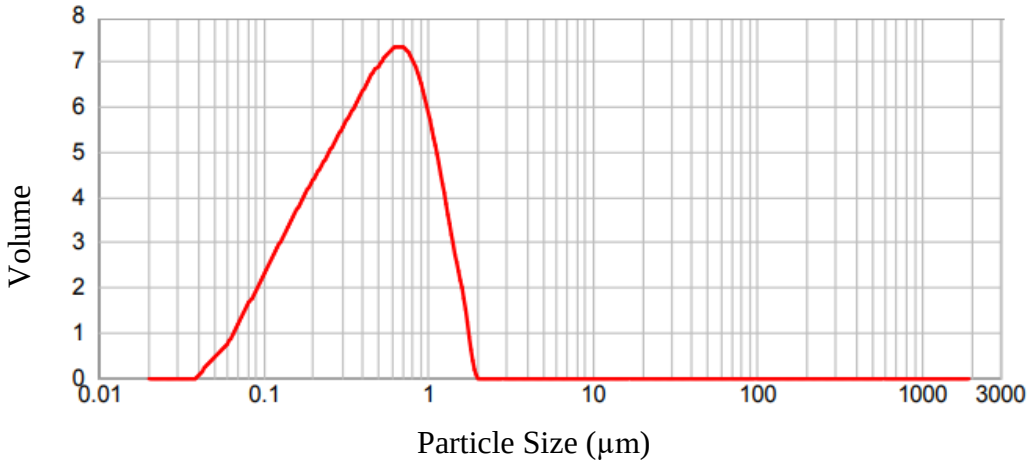

Figure 20. Particle size distribution histogram of the TiO_2 starting powder.

It should be noted that there is a margin of error in the measurements due to agglomeration of the powders. Although an ultrasonic bath was applied to disperse the agglomerates before the particle size distribution analysis, agglomeration of the particles was not completely inhibited. The particle size distribution analysis suggested that size reduction of the particles in all of the starting powders was necessary for better sintering. Ball milling was applied to mix the starting powders homogeneously and to reduce the size of the particles.

4.1.2 X-Ray Diffraction (XRD) Analysis

The XRD pattern of the MgO starting powder is presented in Figure 21. All 2θ values of the main peaks agree with the XRD peak positions of the MgO phase proven in International Centre for Diffraction Data (ICDD) base. The ICDD data base (DB) card number 00-071-1176 suggests that the material is periclase (MgO) that has cubic crystal structure with Fm-3m space group. The characteristic peaks belonging to the (111), (200), (220), (222), and (311) planes of pure MgO were detected at 2θ angles of 36.9°, 42.9°, 62.3°, 74.6°, and 78.6°, respectively. The findings were comparable with the results publicized by Balakrishnan et al. [46].

The peak locations in DB card number 00-071-1176 and in the XRD pattern of the MgO starting powder are almost the same suggesting that the material is polycrystalline cubic structure of MgO. The minor phase detected in the XRD pattern, besides MgO, is magnesite, $Mg(CO_3)$ with the ICDD DB card number 00-086-2346. The card states that $Mg(CO_3)$ has a hexagonal crystal structure with the R-3c space group. The characteristic peaks located at 2θ of 32.6°, 35.9°, 42.9°, 46.8°, and 53.9° were attributed to the (104), (006), (113), (202), and (116) planes, respectively of the $Mg(CO_3)$ phase. Similar results have been reported also by Choi et al. [47] $Mg(CO_3)$ phase present in the MgO starting powder since it was produced by calcination of $Mg(CO_3)$. Although $Mg(CO_3)$ phase seems as impurity, it does not introduce any chemical heterogenity to the products since it decomposes and converts to MgO during the high temperature production processes.

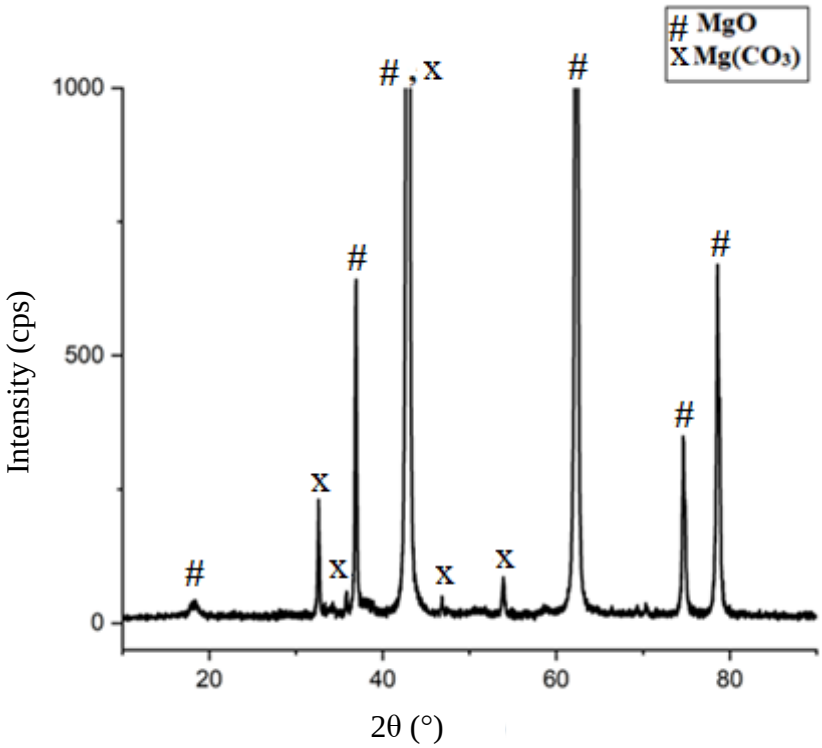

Figure 21. XRD pattern of the MgO starting powder.

The XRD pattern of the TiO_2 starting powder is shown in Figure 22. The ICDD DB card number 00-084-1286 suggests that the powder is anatase phase of TiO_2 with a tetragonal crystal structure. No impurity phase was identified. The characteristic peaks located at 2θ of 25.4°, 37.9°, 48.1°, 53.9°, 55.1°, 62.8°, 68.8°, 70.4°, and 74.1° correspond to the (101), (112), (200), (105), (211), (204), (116), (220), and (215) planes, respectively, of the phase pure anatase phase. Srinivasu et al. reported similar results on the XRD analysis of TiO_2. [48]

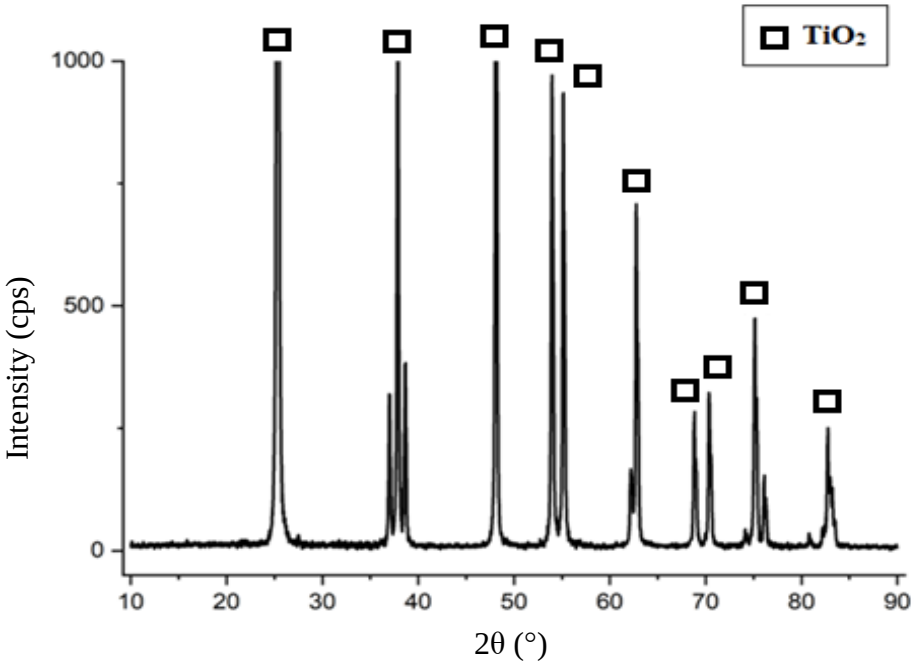

Figure 22. XRD pattern of the TiO_2 starting powder.

The XRD pattern of $CaCO_3$ starting powder is indicated in Figure 23. Single phase was identified as calcite phase, $CaCO_3$, in agreement with the ICDD DB card number 00-086-0174 with hexagonal crystal structure. No impurity phase was detected. The XRD peaks diffracted from (012), (104), (110), (113), (202), (016), (018), and (122)

planes located at 2θ of 23°, 29.4°, 35.9°, 39.4°, 43.1°, 47.1°, 48.5°, and 57.4° are attributed to calcite phase. Render et al. [49] reported comparable results. In the XRD pattern, the $CaCO_3$ starting powder has nearly identical peak angels presented in DB card number 00-086-0174.

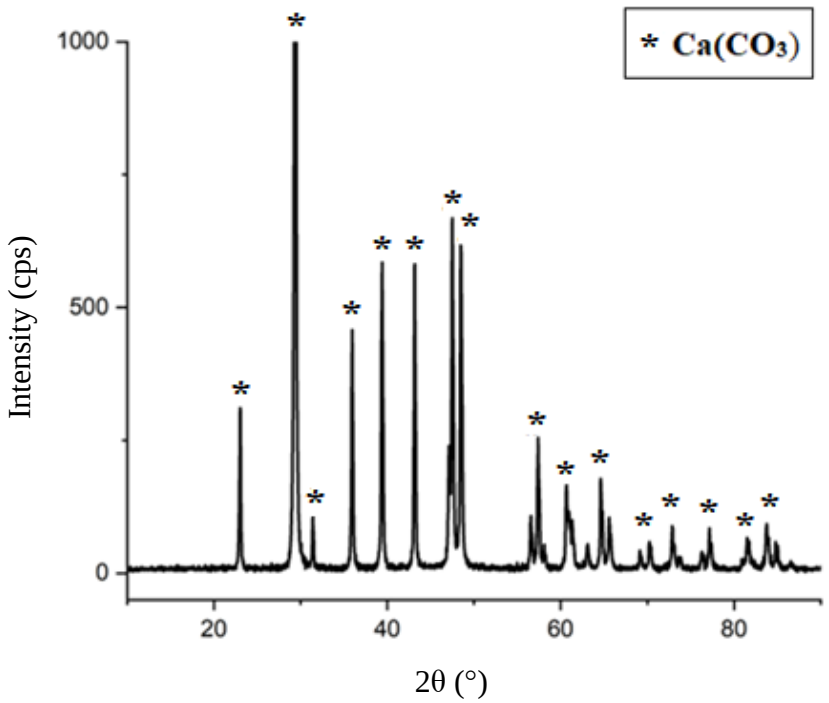

Figure 23. XRD pattern of the $CaCO_3$ starting powder.

4.1.3 SEM Analysis

Tpical SEM images taken at 1000X for the MgO, TiO_2, and $CaCO_3$ starting powders are shown in Figure 24. SEM image of the MgO starting powder, represented in Figure 24 (a), suggests that the powder has a wide size range of particles ranging from 1 to 30 µm. This image supports the particle size distribution analysis data obtained for the MgO starting powder. No significant but partial agglomeration was evident in the MgO starting powder. The particles are irregular in shape.

SEM examination revealed that the TiO_2 starting powder includes particles from nanometer to micrometer size as shown in the image in Figure 24 (b). The powder have a wide range of particles ranging from 0.01 to 70 μm. The size of the particles in this image and that obtained from particle size distribution analysis, shown in Figure 20, are somewhat different from each another. It is obvious that this powder had a lot of agglomerates whereas, the ultrasonic bath used before the particle size distribution analysis successfully dispersed the agglomerates. The TiO_2 particles are irregular in shape.

The SEM image shown in Figure 24 (c) exhibits that the $CaCO_3$ starting powder has particles with various sizes less than 15 μm ranging from 1 to 15 μm. SEM examination revealed that the $CaCO_3$ particles are irregular in shape and show a uniform distribution. Particle size distribution analysis data obtained for the $CaCO_3$ starting powder was confirmed by the SEM examinations.

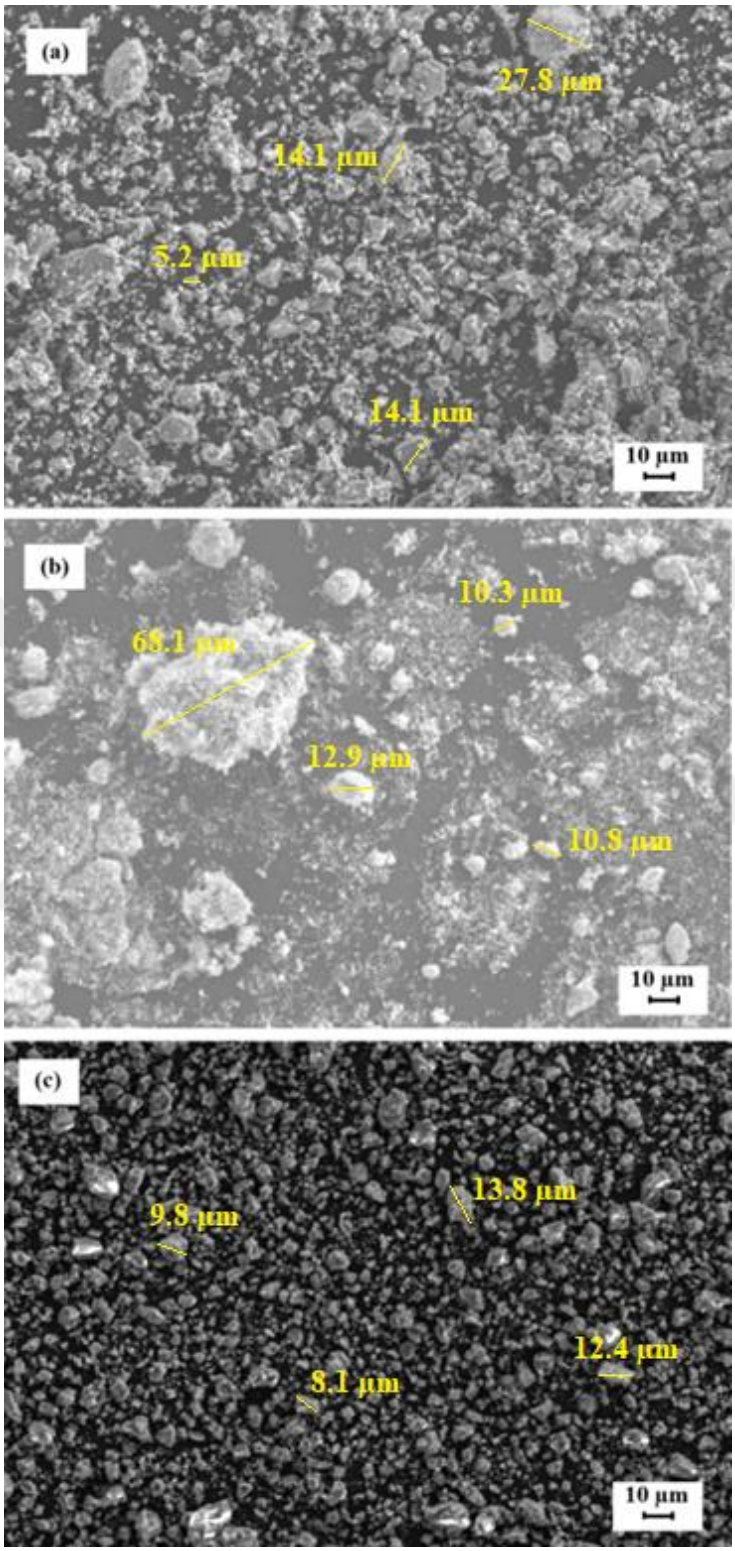

Figure 24. SEM images of the (a) MgO, (b) TiO_2, and (c) $CaCO_3$ starting powders. (1000 X)

4.1.4 EDS Analysis

The EDS spectrum of the MgO starting powder is represented in Figure 25. The EDS analysis indicated that the MgO starting powder composed of only Mg and O elements. No impurity element was detected. EDS analysis revealed that the atomic percentage of Mg and O is close to each other, implying that MgO is the only oxide in this powder. EDS analysis confirms the results of the XRD analysis of the MgO starting powder.

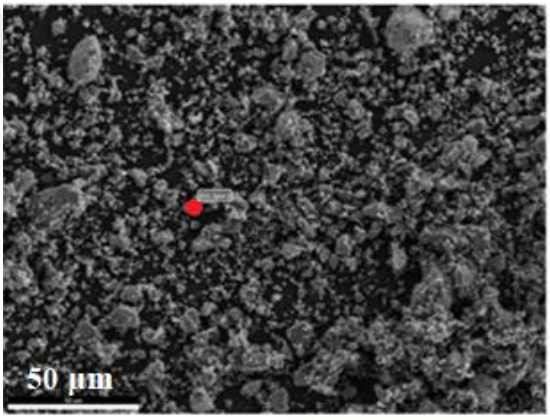

Element Symbol	Atomic Concentration (%)
O	48.47
Mg	51.53

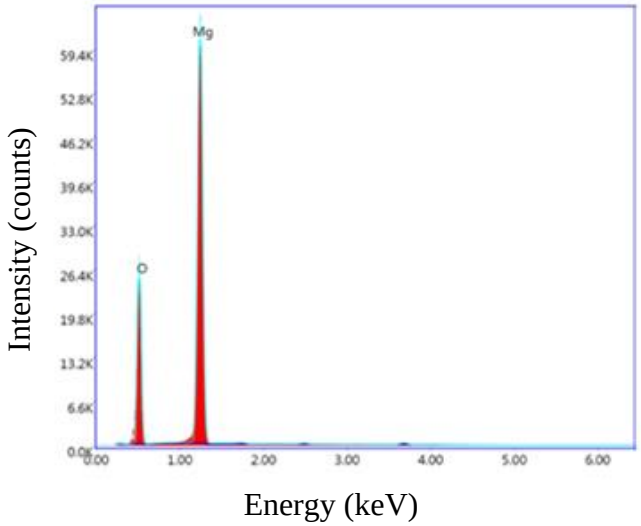

Figure 25. EDS spectrum of the MgO starting powder. The EDS analysis was taken at the spot shown in red color in the SEM image.

The EDS spectrum of the TiO_2 starting powder is shown in Figure 26. The EDS analysis indicated that the TiO_2 powder composed of Ti and O elements. No impurity element was detected. EDS analysis revealed that the atomic percentage of O to Ti is approximately 2, implying that TiO_2 is the only oxide in this powder. EDS analysis confirms the results of the XRD analysis of the TiO_2 starting powder.

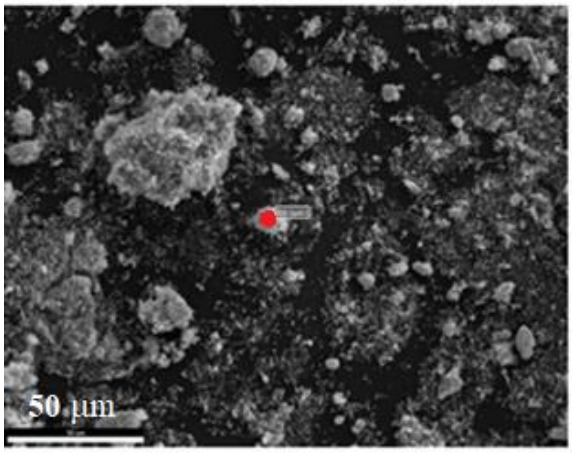

Element Symbol	Atomic Concentration (%)
O	70.6
Ti	28.4

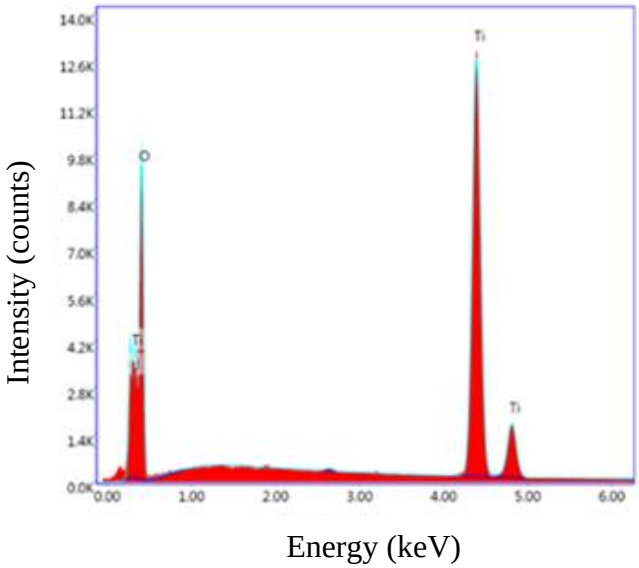

Figure 26. EDS spectrum of the TiO_2 starting powder. The EDS analysis was taken at the spot shown in red color in the SEM image.

The EDS spectrum of the $CaCO_3$ starting powder is shown in Figure 27. The EDS analysis indicated that the $CaCO_3$ starting powder composed of Ca, C, and O elements. No impurity element was detected. EDS analysis revealed that the atomic percentage of C and Ca is close to each other, and the atomic percentage of O to C element is approximately 3 implying that $CaCO_3$ is the only oxide in this powder. EDS analysis confirms the results of the XRD analysis of the $CaCO_3$ starting powder.

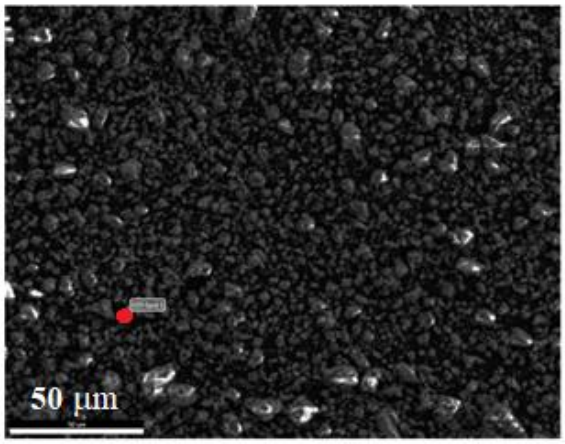

Element Symbol	Atomic Concentration (%)
O	57.76
Ca	24.18
C	18.06

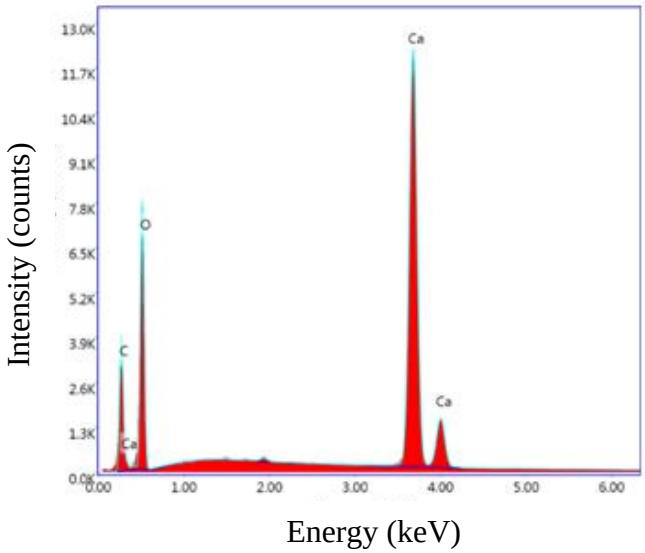

Figure 27. EDS spectrum of the $CaCO_3$ starting powder. The EDS analysis was taken at the spot shown in red color in the SEM image.

4.2 Characterization of the Calcined M0.95CT Powder

4.2.1 Particle Size Analysis

M0.95CT powder was prepared as described in Section 3.1. The particle size distribution of the M0.95CT powder calcined twice at 1050 ºC and ball milled for 7 h was narrow and unimodal as shown in Figure 28. The average particle size of the powder is 1.602 µm. The values of d_{10} and d_{90} are 0.957 µm and 2.730 µm, respectively.

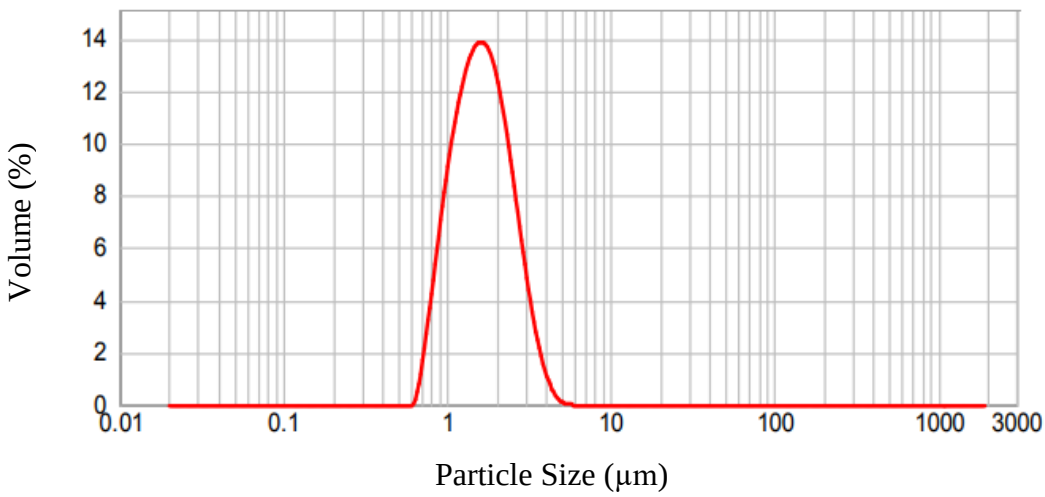

Figure 28. Particle size distribution histogram of the M0.95CT powder.

4.2.2 XRD Analysis

XRD analysis of M0.95CT powder was performed in pellet form as well as in powder form. The XRD patterns were illustrated in Figure 29. Both patterns exhibited diffraction peaks for $MgTiO_3$ (PDF Code: 00-079-0831), $CaTiO_3$ (PDF Code: 00-082-0229), and $MgTi_2O_5$ (PDF Code: 00-089-6945). It is obvious that less number of diffraction peaks was detected when the XRD analysis was done in pellet form. The characteristic peaks of $MgTiO_3$ at 20.8°, 23.1°, 32.8°, 35.4°, 40.6°, 49.1°, 53.6°, 56.9°, 61.7°, and 63.7° belong to (101), (012), (104), (110), (113), (024), (116), (018), (214), and (300) planes, respectively. Wang et al. [50] attributed the five highest diffraction peaks appearing at 2θ of 32.89°, 35.50°, 40.64°, 49.16°, and 53.65°to (104), (110), (113), and (024), and (116) planes for $MgTiO_3$. The characteristic peaks located at 23.1°, 32.8°, and 47.4° correspond to the (101), (121), and (202) planes, respectively of the $CaTiO_3$ phase. The $CaTiO_3$ peak locations and intensities coincided well with the standard XRD data of orthorhombic $CaTiO_3$ included in the study of Han et al. [51] The characteristic peaks at 25.4°, 31.4°, 32.7°, 36.8°, 41.4°, 46.3°, 48.7°, 52.4°, 55.3°, and 59.9° belong to (101), (121), (230), (131), (420), (430), (002), (341), (060), and (351) planes, respectively of $MgTi_2O_5$. The findings are comparable with those reported by Nakagoshi and Suzuki [52].

The intensities of the XRD peaks for the unreacted MgO and TiO_2 phases were extra when XRD was taken in powder form. This finding implies that the quantities of the unreacted MgO and TiO_2 phases are more as the calcination is done in powder form. For that reason, the calcination procedure was carried out in pellets since this way offers high atomic packaging and increases the possibility of phase transformation. As the calcination is done in the pellet form, XRD analysis detected $MgTiO_3$ as primary crystalline phase along with $CaTiO_3$ and $MgTi_2O_5$ as minor crystalline phases.

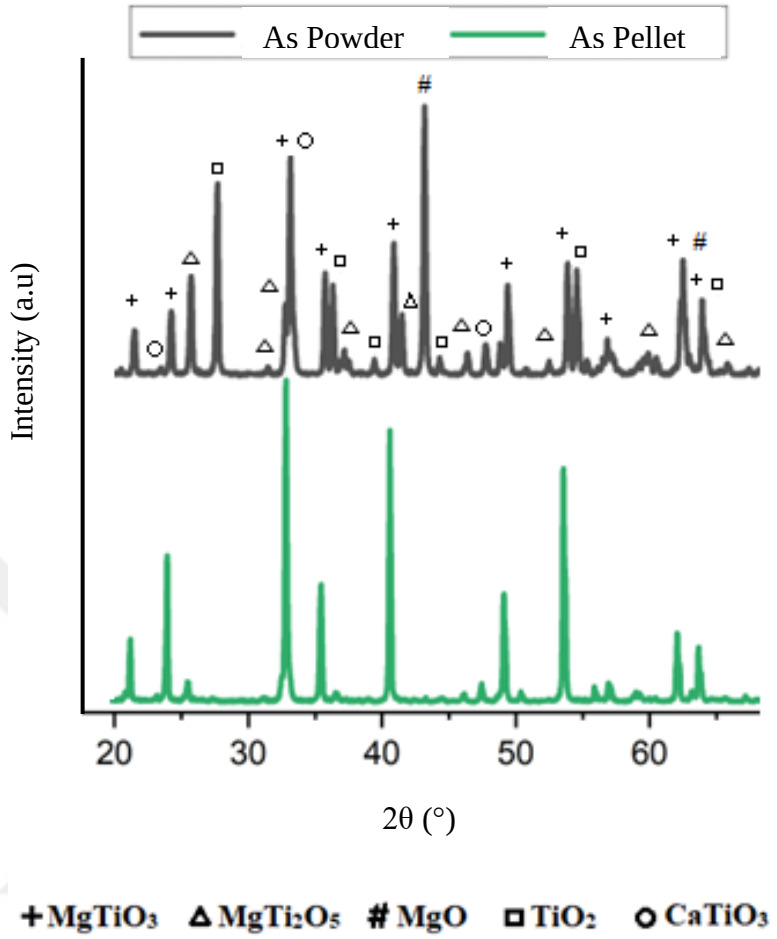

Figure 29. XRD patterns of M0.95CT powder.

The existence of two distinct phases, $MgTiO_3$ and $CaTiO_3$, is an indication that no solid solution formed between them. Wang et al. [2] concluded that $MgTiO_3$ (ilmenite structure) and $CaTiO_3$ (perovskite structure) do not form a solid solution because of their distinct crystal structures. Also, due to their significantly different ionic sizes (Mg^{2+} is 0.72 Å and Ca^{2+} is 1.00 Å), $MgTiO_3$ and $CaTiO_3$ cannot be mixed. [53] The second calcination is needed to ensure the reaction of the unreacted phases and to eliminate the presence of the undesired $MgTi_2O_5$ phase. The XRD patterns of M0.95CT ceramics taken after the 1st and 2nd calcination were shown in Figure 30. The XRD pattern of the pressureless sintered M0.95CT ceramic is also

included in Figure 30 for comparison purpose. The features of this pattern will be discussed in the next section.

A comparison of the XRD patterns taken after the 1st and 2nd calcination revealed that, as predicted, the unreacted TiO_2 phase has completely disappeared. Even though the intensity of the unreacted MgO phase decreased, the peaks for the MgO phase were still existent implying that there is still an excess of it in the calcined M0.95CT ceramic. Unreacted MgO phase leads to formation of undesired $MgTi_2O_5$ phase. It is commonly known that $MgTi_2O_5$ phase is easily produced during mixed oxide synthesis and is difficult to eliminate entirely. Yu et. al. [54] suggested that by raising the Mg/Ti ratio to a value slightly higher than 1.27, the formation of $MgTi_2O_5$ phase can be inhibited but, in this circumstance due to the presence of excess MgO, Mg_2TiO_4 phase forms as a second phase. Since the Mg/Ti ratio in this study was less than 1.27, Mg_2TiO_4 phase was not detected in the XRD patterns.

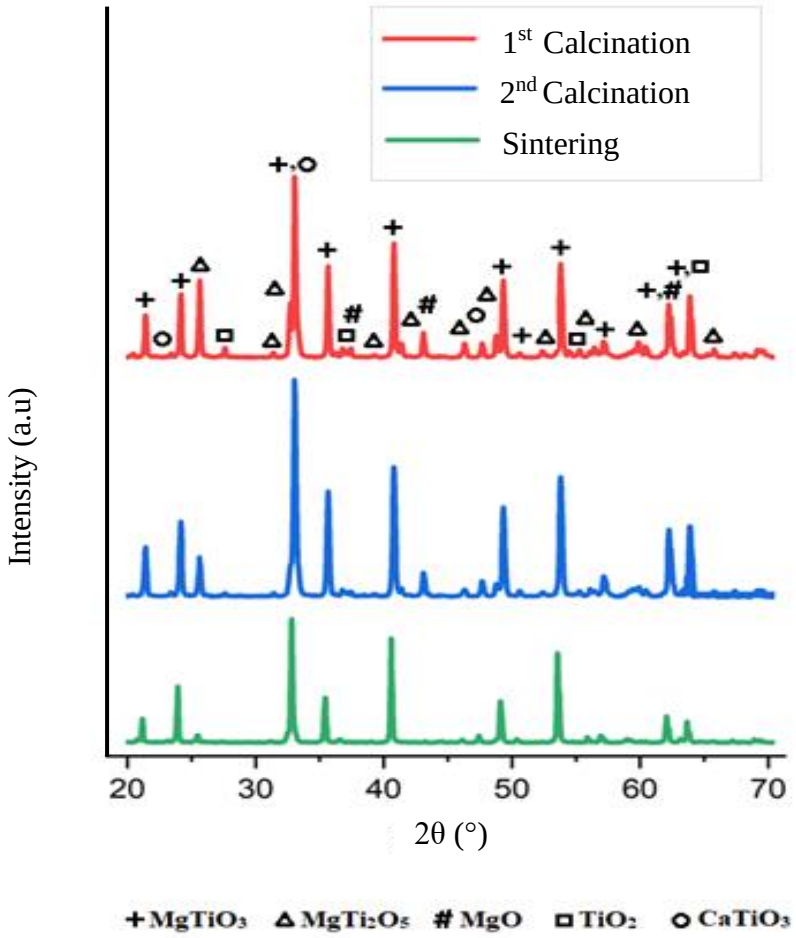

Figure 30. XRD patterns of M0.95CT ceramic. The patterns were taken after the 1st calcination, 2nd calcination, and pressureless sintering at 1400 °C.

4.3 Effect of Green Density

Green density of M0.95CT pellets was determined as described in Section 3.1. The effect of applied pressure on the relative green density is shown in Figure 31. The lowest green density was obtained at applied pressure of 80 MPa. An increase in green density was observed as the applied pressure is increased. It can be interpreted that, for each applied pressure, interparticle pores are reduced as a result of the

rearrangement of particles and filling the available space. Also, particle deformation started at particle-particle contact points. Because of the high degree of packing and little room for rearrangement, the increase in density achieved at applied pressures is small. It is obvious that the increase in density slows down at pressures of 200 and 240 MPa. It can be interpreted that the compact ceramic deformed elastically. If this elastic deformation happens, the ejection force or pressure required to remove the compact ceramic rises. Therefore, increase in density at higher applied pressures is low. As a result, 120 and 160 MPa pressure was determined to be the most appropriate pressures for the compaction.

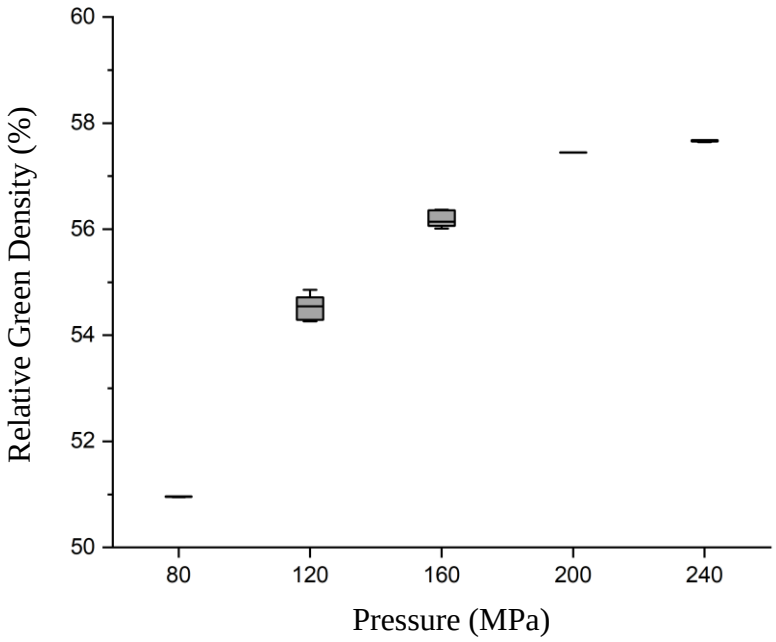

Figure 31. Variation in the relative green density with applied pressure.

The effect of the pressure applied for the formation of the green body on the densification of M0.95CT ceramic is shown in Figure 32. It is evident that 120 MPa leads to the best shrinkage occurrance during sintering. The shrinkage value calculated for 120 MPa pressure is around 20.85 %. Therefore, this pressure was applied to shape all M0.95CT ceramics.

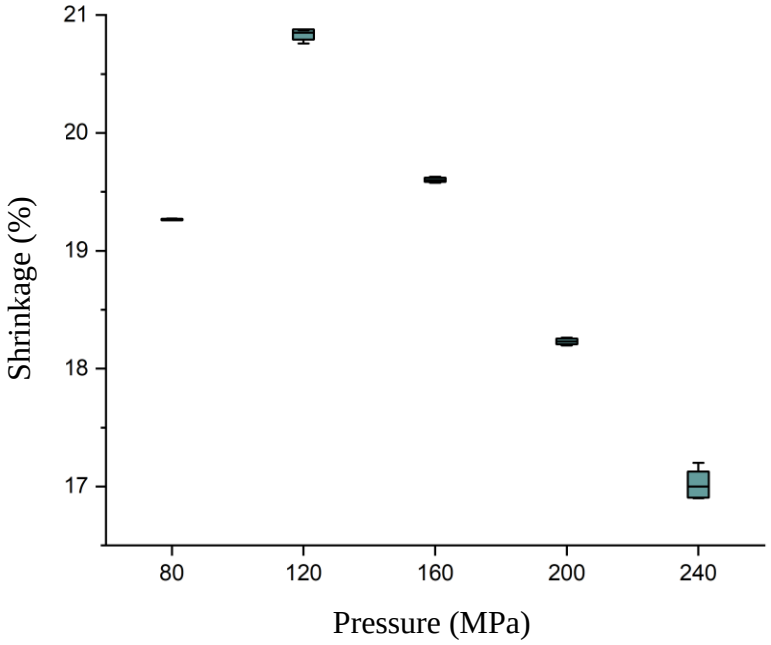

Figure 32. Variation in shrinkage occurred during sintering at M0.95CT ceramic with applied pressure.

4.4 Sintering of M0.95CT Ceramics

4.4.1 Characterization of Pressureless Sintered M0.95CT Ceramic

4.4.1.1 XRD Analysis

M0.95CT pellet was pressureless sintered as described in Section 3.1. The XRD patterns of the M0.95CT ceramic sintered at 1300, 1350, and 1400 °C for 1 h are shown in Figure 33. Same sintering schedule was applied to all ceramics sintered at three different sintering temperatures. The $MgTi_2O_5$ phase was detected in all M0.95CT ceramics. Intensity of the $MgTi_2O_5$ phase slightly decreased with increasing sintering temperature. This finding suggests that there is not much but, a noticeable decrease in the quantity of $MgTi_2O_5$ phase. Further research is needed to quantify the $MgTi_2O_5$ phase present after each sintering practice.

Negligibly small peak for the unreacted TiO_2 was detected in the pattern of the M0.95CT ceramic sintered at 1300 °C implying that 1300 °C is not a proper temperature for sintering. The presence of a small peak for the unreacted TiO_2 might result in preferred orientation and different XRD intensity since only a single peak of TiO_2 was detected. $MgTiO_3$ appeared as the essential crystalline phase whereas, $CaTiO_3$ and $MgTi_2O_5$ were detected as secondary phases in the patterns of the M0.95CT ceramics sintered at all temperatures. Results comply with those gathered for the calcined M0.95CT powder.

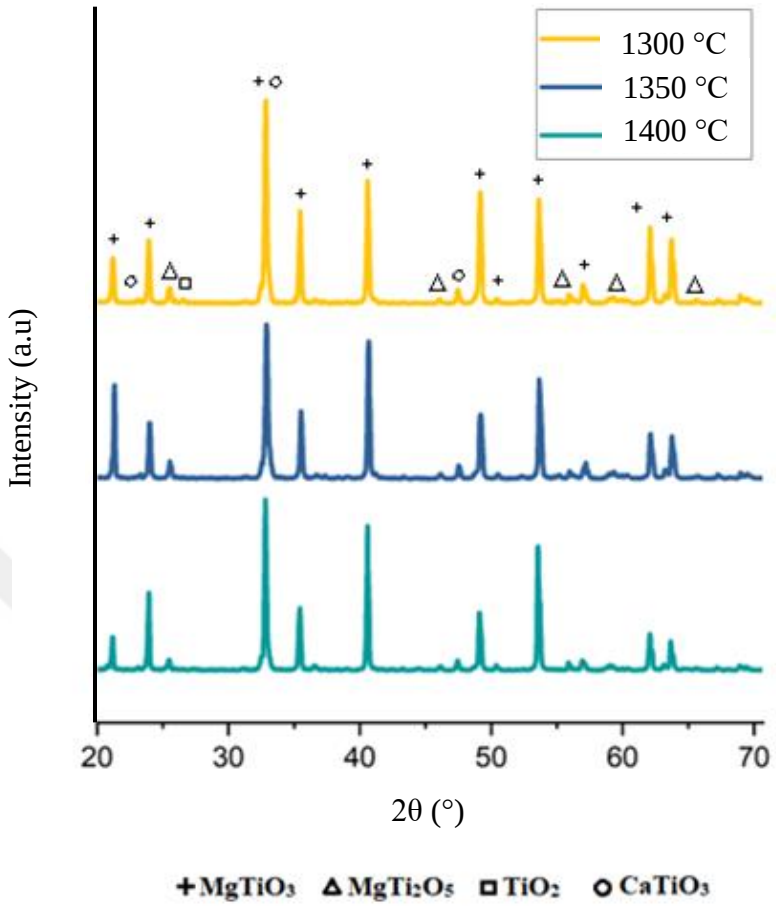

Figure 33. XRD patterns of the M0.95CT ceramic pressureless sintered at 1300, 1350, and 1400 °C.

4.4.1.2 SEM Analysis

The representative SEM images for the thermally etched M0.95CT ceramics pressureless sintered at 1300, 1350, and 1400 °C are represented in Figure 34. For oxide ceramics, thermal etching is frequently utilized. Etching temperature is typically 150 °C below sintering temperatures. Depending on the structure and composition of the grain boundary, the etching period might range from 15 minutes to several hours. [55] In the present study, M0.95CT ceramics were thermally etched

at 1150, 1200, and 1250 °C for 15 min for the samples pressureless sintered at 1300, 1350, and 1400 °C, respectively. Figure 34 (a) reveals that eventhough the intergranular pore area decreased due to particle contact points and particle deformation, sintering at 1300 °C was incomplete. There are a large number of tightly spaced pores on grain boundaries. The pore forms at the beginning of an asymmetrical network of interconnected channels.

When the sintering temperature was increased to 1350 °C, the morphology of M0.95CT ceramic changed as shown in Figure 34 (b). It is obvious that the driving force required for sintering is more efficient at 1350 °C than at 1300 °C. The amount of the pores decreased and the size of the pores became smaller. Matrix phase, predicted to be $MgTiO_3$, and other secondary phases ($CaTiO_3$ and $MgTi_2O_5$) were observed clearly. The SEM image of the thermally etched M0.95CT ceramic pressureless sintered at 1400 °C is shown in Figure 34 (c). The development of isolated and spherical pores were observed. The second phases formed within the grain and at the grain boundaries became more visible compared to the SEM image of the M0.95CT ceramic sintered at 1350 °C. Grain sizes increased and reached to approximately 30-40 μm for the matrix phase implying that significant amount of grain growth took place during densification.

In order to see whether the grain size distribution is homogeneous, another SEM image taken at a lower magnification (1250 X) for the thermally etched M0.95CT ceramic pressureless sintered at 1400 °C. The image is shown in Figure 35. The uniform small and cuboid shaped $CaTiO_3$ grains are located at the grain boundaries and inside the $MgTiO_3$ grains. Larger and irregular shaped grains were $MgTiO_3$ and $MgTi_2O_5$. It can be concluded that the M0.95CT ceramic pressureless sintered at 1400 °C has nonuniform grains in terms of matrix structure. Also, abnormal grain growth was observed in some areas. Jawahar et al. [11] reported that strength of ceramics decreases by abnormal grain size and grain growth. Also, Wang et al. [2] stated that grain size in ceramics contribute to extrinsic loss. The effects of grain size developed during sintering on dielectric properties will be evaluated in the forthcoming section.

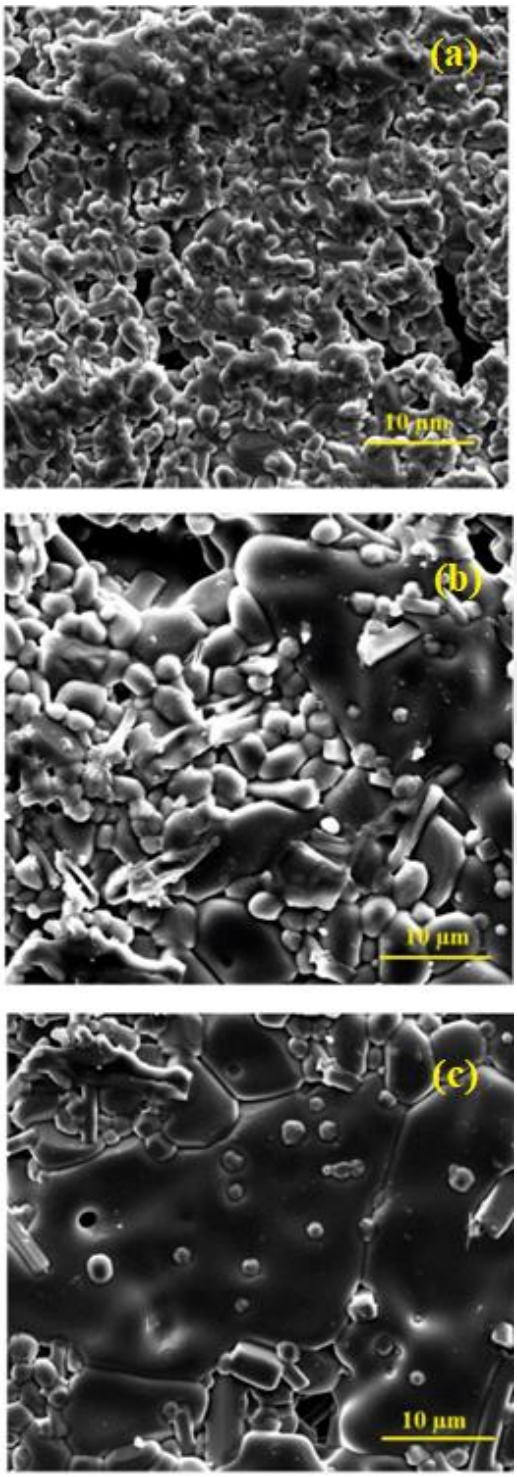

Figure 34. SEM images of the thermally etched M0.95CT ceramics pressureless sintered at (a) 1300, (b) 1350, and (c) 1400 °C. (2500 X)

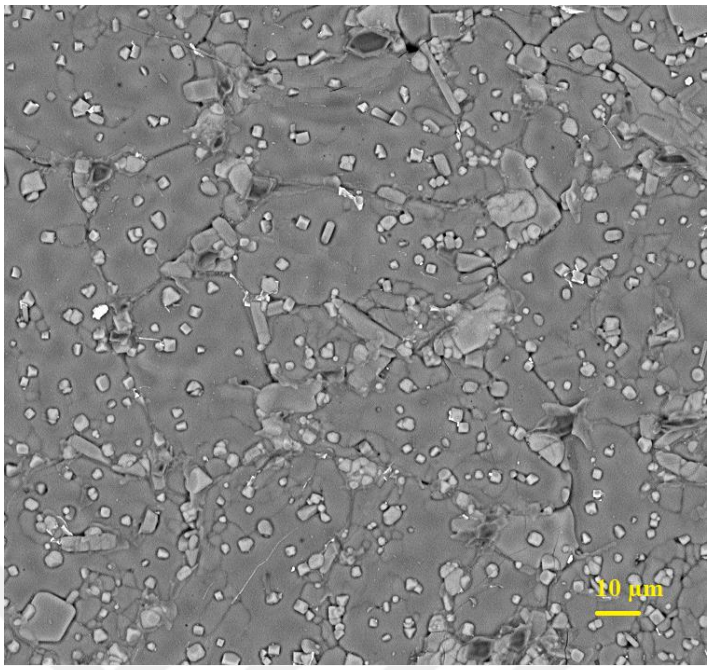

Figure 35. SEM image of the thermally etched M0.95CT ceramic pressureless sintered at 1400 °C. (1250 X)

The backscatter detector (BSD) of SEM was employed to take BES-SEM image for the thermally etched M0.95CT ceramic pressureless sintered at 1400 °C. The image is shown in Figure 36. The XRD analyses revealed that there is more than one phase in the ceramic. Thanks to the BSD, with the help of mass contrast of elements, information about the phase distributions and shapes in the microstructure can be obtained. Table 2 includes the atomic concentration of each element identified in the microstructure presented in Figure 36. Gold (Au) was neglegted in the phase analysis. Oxygen (O) was also ignored during phase analysis because, in general, the poor sensitivity of EDS analysis makes it challenging to measure light components. [56] The atomic concentration of O element confirms this interpretation. Analyzing the atomic concentration of the elements present at Point A reveals that the atomic percentages of Mg and Ti are close to each other. The phase at Point A can be interpreted as matrix phase, $MgTiO_3$. The atomic concentration of the elements present at Point B suggests that Ti to Mg ratio is close to 2. The phase at Point B is attributed to $MgTi_2O_5$. This phase consists of an orthorhombic crystal system with a

different geometry on each side. It is located at the grain boundaries of $MgTiO_3$ in the structure and exhibited a partially homogeneous distribution. The whitest spots in the image, Point C, belong to $CaTiO_3$ phase since the ratio between the Ca and Ti is approximately 1. $CaTiO_3$ phase positioned at the grain boundaries as well as within the grains as shown in Figure 36. Ferreira et al. [10] also reported that $CaTiO_3$ is located at triple spots between grains of $MgTiO_3$.

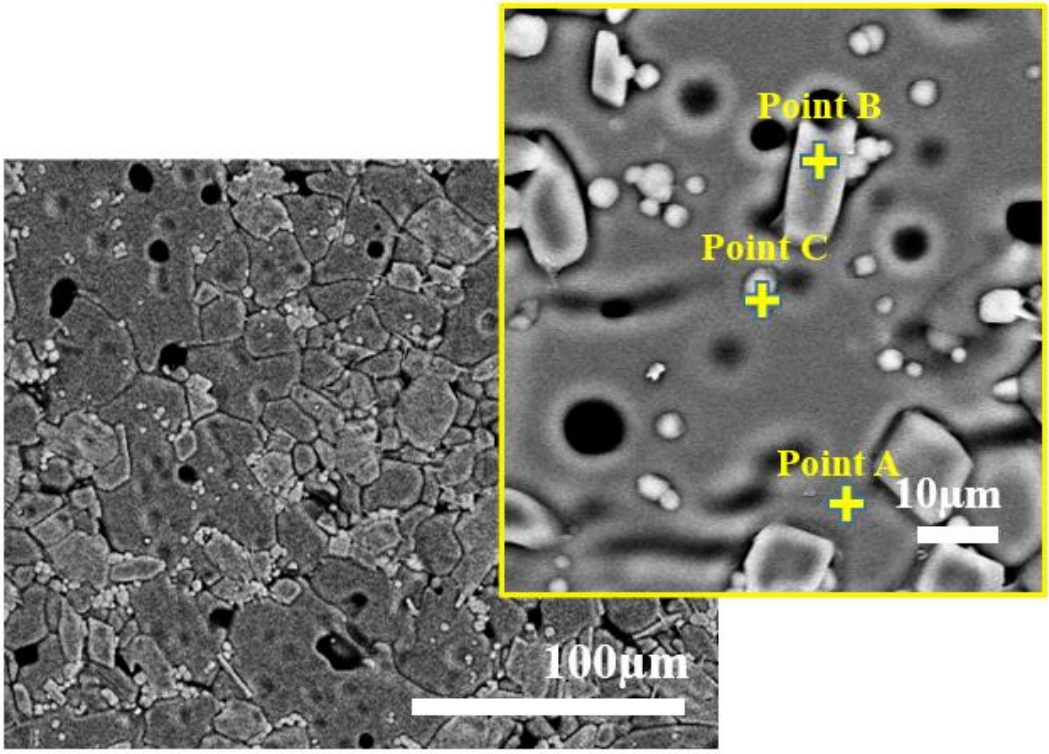

Figure 36. BSD-SEM image of the thermally etched M0.95CT ceramic pressureless sintered at 1400 °C.

Table 2. EDS analysis of the thermally etched M0.95CT ceramic pressureless sintered at 1400 °C. The analysis was done at different points shown in Figure 36.

Element Symbol	**Atomic Concentration (%)**		
	Point A	**Point B**	**Point C**
O	20.73	13.47	13.38
Mg	35.57	28.1	8.11
Au	2.06	2.23	2.23
Ca	2.07	0.97	33.26
Ti	39.56	55.22	43.02

4.4.2 Characterization of M0.95CT-HIP Ceramic

4.4.2.1 XRD Analysis

XRD patterns taken before and after the application of HIPing for the M0.95CT ceramics pressureless sintered at 1400 °C are shown in Figure 37. In both patterns, $MgTiO_3$ is the primary crystalline phase while, $CaTiO_3$ and $MgTi_2O_5$ present as secondary phases. The intensity of the unwanted $MgTi_2O_5$ phase was almost the same in both patterns, implying that the quantity of $MgTi_2O_5$ phase did not change much after HIPing.

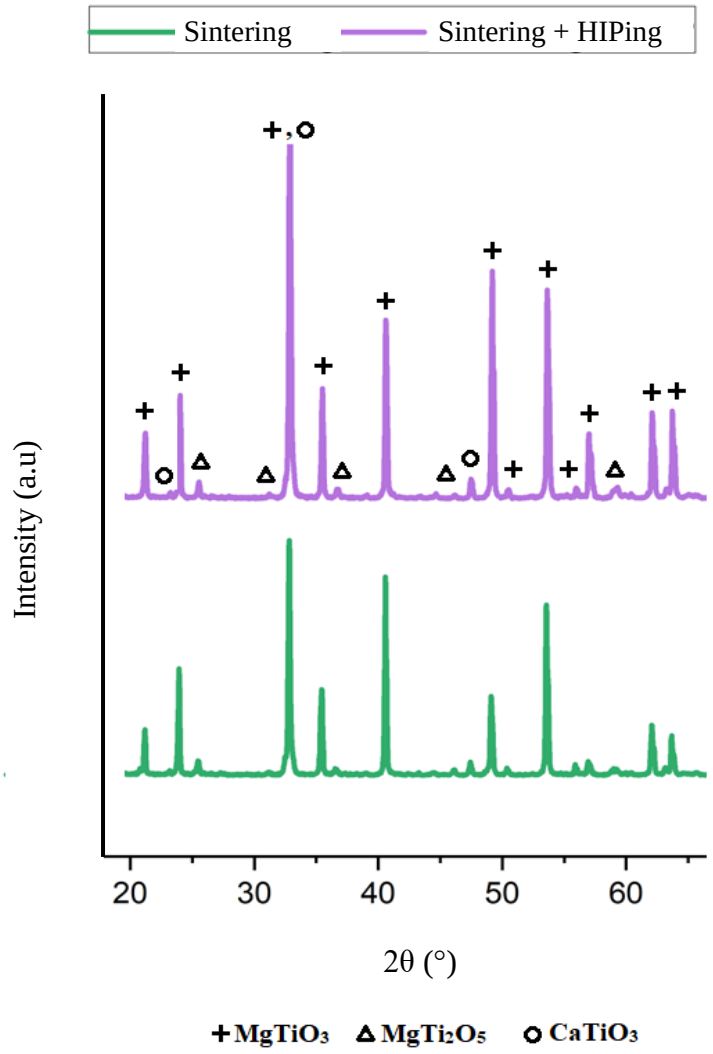

Figure 37. XRD patterns taken before and after the application of HIPing for the M0.95CT ceramic pressureless sintered at 1400 °C.

It can be stated that after HIPing, there is no noticeable difference in terms of the phases present. However, microstructure (sample orientation) has a significant impact on XRD intensity. [64] Since, crystallites are produced under different condition (during HIPing), their extension will vary. It might lead to preferred orientation, changing XRD intensities of the peaks located at 49.19° and 56.99° belonging to (024) and (018) planes, respectively.

4.4.2.2 SEM Analysis

SEM images taken before and after the application of HIPing for the M0.95CT ceramics pressureless sintered at 1400 °C are shown in Figure 38. Pore amount and size decrease after HIPing.

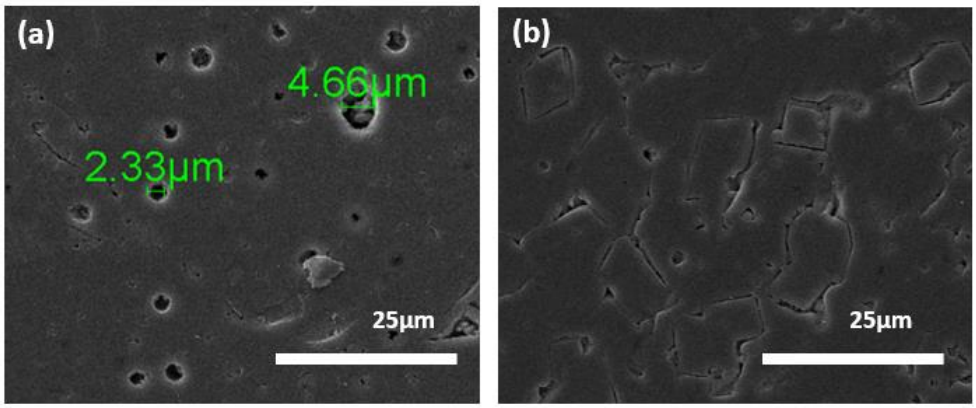

Figure 38. SEM images taken (a) before and (b) after the application of HIPing for the M0.95CT ceramics pressureless sintered at 1400 °C. (2000 X)

Similar microstructures have been reported also by Filipovic et al. [13] for the $MgTiO_3$ ceramics as shown in Figure 39. In their study, HIPing was applied at 1200 °C for 2 h in Ar atmosphere at a pressure of 200 MPa. Grain growth and a small amount of spherical pores are the main features of the images. It is obvious that much lower porosities and much compact structure was achieved as a result of HIPing.

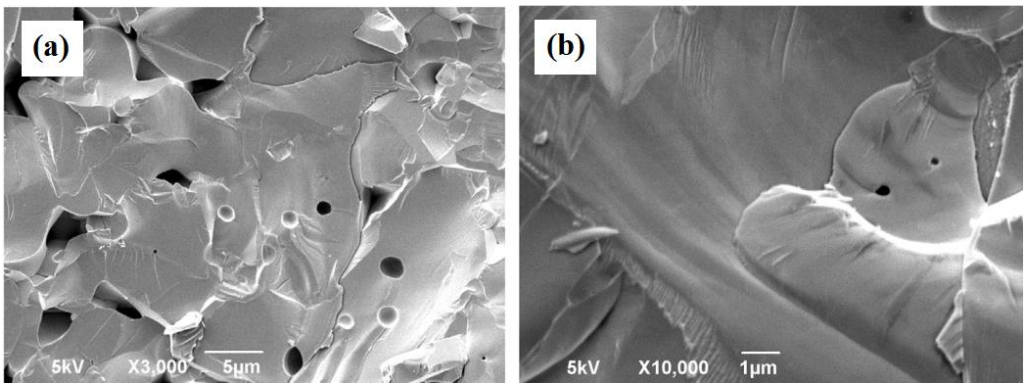

Figure 39. SEM images of $MgTiO_3$ ceramic (a) before HIPing, and (b) after HIPing. [13]

Moreover, as shown in Figure 15, color of the M0.95CT ceramic pellets pressureless sintered at 1400 °C changed from light brown to dark black after HIPing at 1200 °C for 1 h. The reason why a color change took place after HIPing is interpreted as a lack of oxygen and a high concentration of flaws due to inert argon atmosphere. [66] Moulson and Herbert [71] also supports this attitude by stating that cations like Mg^{2+}, Al^{3+}, Fe^{3+}, and Ca^{2+} that substitute on Ti^{4+} sites to create acceptors make up the majority of $BaTiO_3$'s main impurities. The oxygen vacancies that result try to compensate the charge deficiency.

4.4.3 Properties of Pressureless Sintered M0.95CT Ceramics

4.4.3.1 Density

The relative to theoretical density of the M0.95CT-HIP and the M0.95CT ceramics pressureless sintered at 1300, 1350, and 1400 °C for 1 h is shown in Figure 40. The density of M0.95CT-HIP ceramic is included for comparison purpose and will be discussed later in Section 4.4.4.1. Four measurements were taken into considiration to establish a reliable data for the density of the M0.95CT ceramics sintered at each temperature. Since the determinations at 1400 °C are more consistent with each

other, the data points overlap. The theoretical density of the M0.95CT ceramics pressureless sintered at 1300 °C is the lowest, with an average of 91.05% ± 0.38 %. The ± signs next to the determination point represent the standard deviation. The M0.95CT ceramic pressureless sintered at 1400 °C has the highest relative density, with an average of 96.06% ± 0.27%. Huang and Weng [45] stated that M0.95CT ceramics required sintering at temperatures as high as 1400 °C. Lower densities were obtained for lower sintering temperatures because of insufficient diffusion rates. Therefore, 1400 °C is selected as pressureless sintering temperature for the rest of the study.

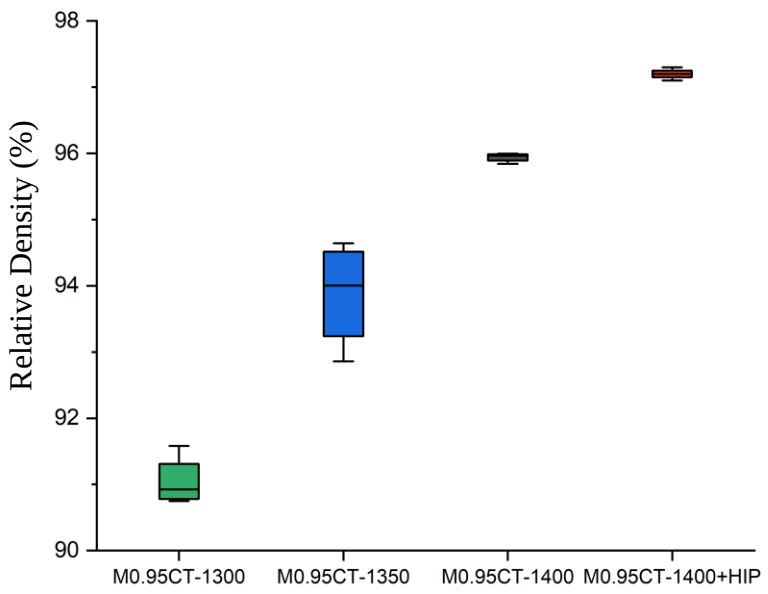

Figure 40. Relative density for the M0.95CT ceramics pressureless sintered at different temperatures.

Ferreira et al. [57] reported the relative density of the M0.94CT ceramic sintered at 1400 °C for 4 h as 97%. On the other hand, Örek [19] stated that the M0.95CT ceramics had relative densities of 88%, 96%, 97.5%, and 96% after being pressureless sintered for 4 h at 1200, 1225, 1250, and 1300 °C, respectively. When

all these studies are compared, it can be deduced that other parameters besides the sintering temperature and time have a significant effect on the density of M0.95CT ceramics.

4.4.3.2 Dielectric Constant and Loss

The parallel plate capacitor method, as stated in Section 3.3.2, was used to measure the dielectric constant of M0.95CT ceramics. Variation in ε_r with frequency for the M0.95CT ceramic pressureless sintered at 1400 °C is shown in Figure 41. Three measurements were made at each frequency to establish a reliable data for ε_r values for M0.95CT ceramics. An average ε_r value of 20.58, 20.5, 20.48, and 20.47 was recorded at 1 kHz, 10 kHz, 100 kHz, and 1 MHz, respectively for the M0.95CT ceramic pressureless sintered at 1400 °C. Although ε_r values measured at the same frequency for the M0.95CT ceramic pressureless sintered at different temperatures are quite consistent, there is a slight difference in the ε_r values measured at different frequencies. A slight decrease in ε_r with increasing frequency might be resulted from dielectric polarization mechanism mentioned in Section 2.2.

Zhou et al. [9] reported that the ε_r value of M0.95CT ceramic is approximately 21 at 7 GHz. Also, Huang et al. [58] stated that the lattice parameters, vibration modes, packing density, ionic polarizability, and bond valence related to the intrinsic factors, as well as extrinsic contributions combining the density, second phases, porosity, impurities, surface morphology, and lattice defect would all affect the microwave dielectric properties of ceramics. The change of ε_r may be due to all of these variations.

LCR Meter capacity is suitable only for low frequencies as mentioned Section 3.3.2. Therefore, ε_r values at higher frequencies like 1-3 GHz was verified using the network analyzer with antenna design method.

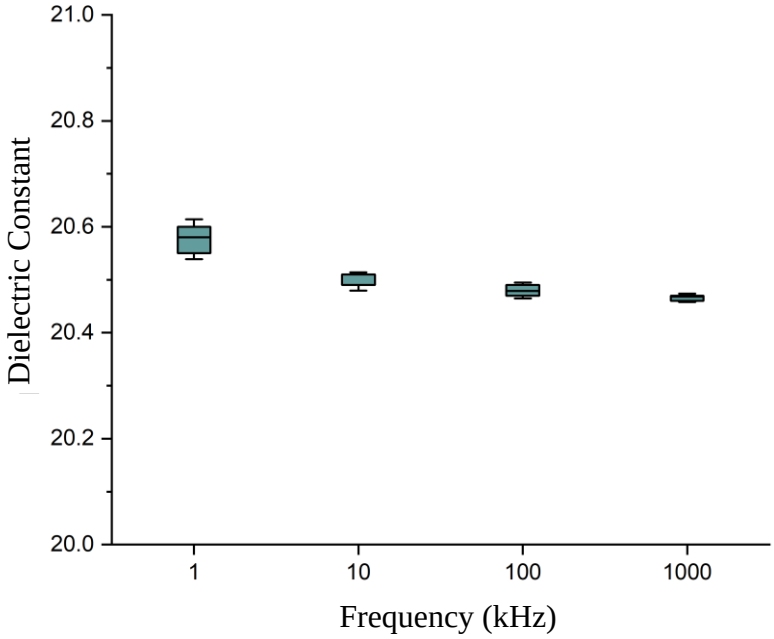

Figure 41. Variation in Ɛr with frequency for the M0.95CT ceramic pressureless sintered at 1400 °C.

The average relative density and Ɛr (at 1 MHz) for the M0.95CT ceramics with pressureless sintered at different temperatures are shown in Figure 42. Both properties show parallel results with each other and the highest value is obtainet for the M0.95CT ceramic pressureless sintered at 1400 °C. It can be concluded that density has a dominant influence on Ɛr. The results confirm Mohamed's [12] argument that a second phase or the grain size have less of an impact than porosity on electrical properties.

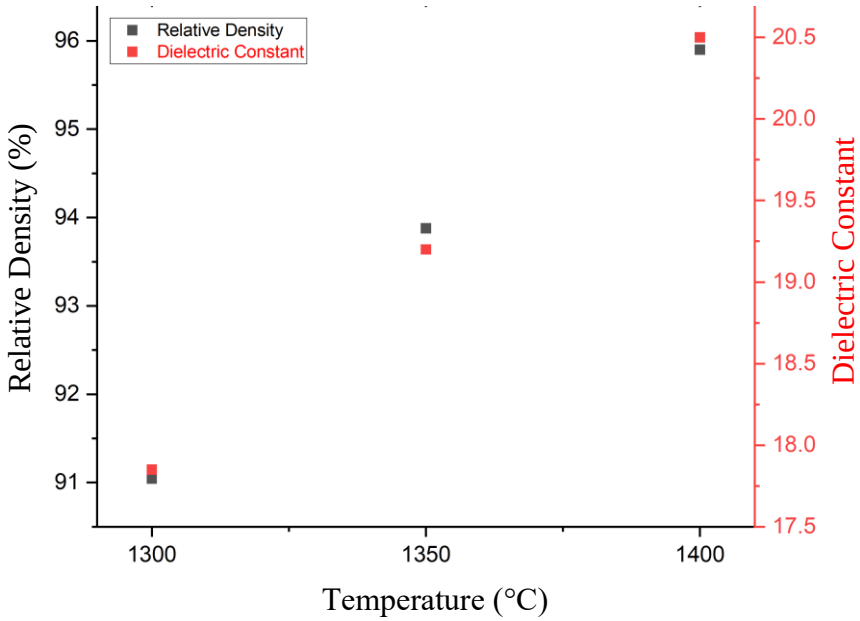

Figure 42. The average relative density and Ɛr (at 1 MHz) for the M0.95CT ceramics pressureless sintered at different temperatures.

Variation in Df with frequency for the M0.95CT ceramic pressureless sintered at 1400 °C is shown in Figure 43. The change in Df with frequency exhibits the same behavior as shown in Figure 5. Df value of the M0.95CT ceramic pressureless sintered at 1400 °C was 0.00332 at 1 MHz. Huang and Weng [59] stated that M0.95CT ceramics may provide typical Qf values 56,000 (at 7 GHz). The Df value obtained is almost 10 times higher than that Huang et al. reported. Since the Df values obtained in their study were not measured at the same frequency, the values may not be compared directly. Oasim et al. [60] reported that the Df value decreases with an increase in frequency. This statement supports the results obtained.

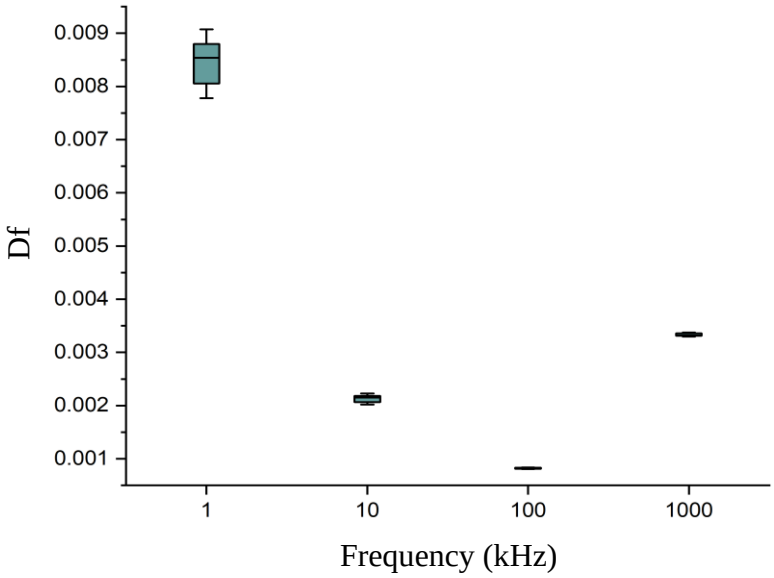

Figure 43. Variation in Df with frequency for the M0.95CT ceramic pressureless sintered at 1400 °C.

4.4.3.3 Resistivity

The variation in resistivity with temperature for the M0.95CT ceramics pressureless sintered at 1400 °C is shown in Figure 44. The measurement could not be taken for this ceramic at temperatures higher than300 °C because no current passed through the ceramic. Since the maximum resistivity value that the device can measure is 200 MΩ.cm , it can be interpreted that the M0.95CT ceramic pressureless sintered at 1400 °C has a very high resistivity greater than 200 MΩ.cm. When the resistance of ceramics are considered in general, Zirconia (ZrO_2) has low resistivity at 10 GΩ.cm, while ultra-pure Al_2O_3 has the greatest resistivity at 20,000 TΩ.cm. [61] It can be concluded that the M0.95CT ceramic pressureless sintered at 1400 °C is a good insulator and dielectric material.

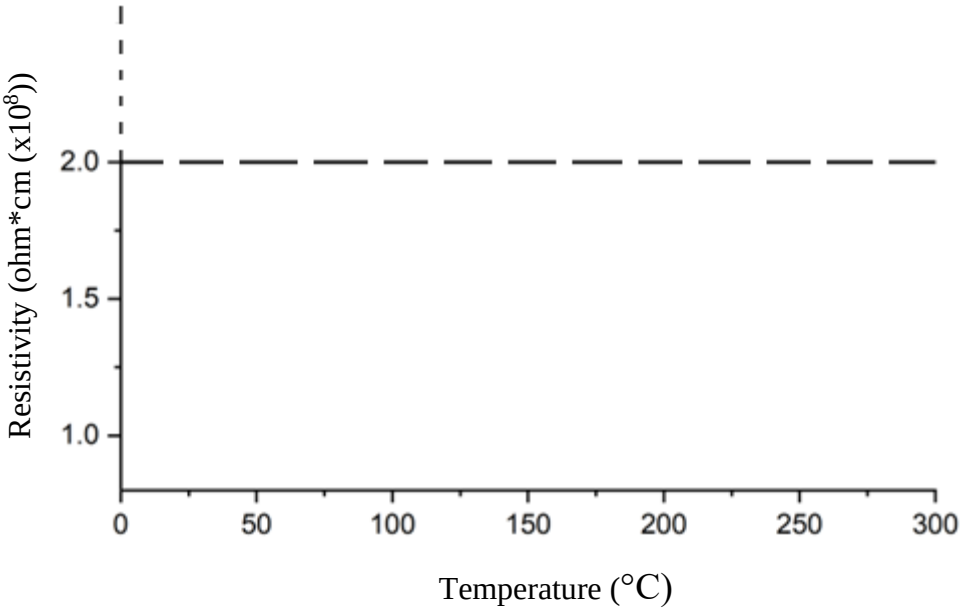

Figure 44. The variation of resistivity with temperature for the M0.95CT ceramic pressureless sintered at 1400 °C.

4.4.4 Properties of M0.95CT-HIP Ceramics

4.4.4.1 Density

The relative densities of M0.95CT and M0.95CT-HIP ceramics are compared in Figure 40. It is obvious that HIPing improves the density of the M0.95CT ceramics pressureless sintered at 1400 °C. The average theoretical density increased from 96.06% ± 0.27% to 97.2% ± 0.36% . The M0.95CT ceramics pressureless sintered at 1400 °C revealed better results in terms of reproducibility. An equal amount of density increase could not be obtained for each of the M0.95CT-HIP ceramic. The ratio difference in closed and open porosities before HIPing may be the reason why the repeatability of M0.95CT-HIP ceramics is lower than that of the M0.95CT ceramics pressureless sintered at 1400 °C.

4.4.4.2 Dielectric Constant and Loss

Variation in Df with frequency for the M0.95CT-HIP ceramic is shown in Figure 45. The average Df value of M0.95CT-HIP ceramic was measured as 0.3717 at 1 MHz. A significant loss in Df of the M0.95CT ceramic pressureless sintered at 1400 °C occurred upon HIPing. Hu et al. [62] claims that the fluctuation of Qf value in microwave dielectrics is affected by a variety of factors, including oxygen vacancy content and impurity phases, anharmonic phonon vibration, order-disorder transition, pore density, and grain size distribution. In a similar study Filipovic et al. [63] stated that the samples sintered using HIP exhibit a notably higher level of disorder as well as increased oxygen vacancy concentrations, by around 40%. The absence of oxygen during HIPing, because Ar gas was used, causes a greater number of oxygen vacancies to appear, which increases the degree of crystal lattice disorder. In line with the comments made, it has been confirmed that the Df value resulting from the HIP application should be high.

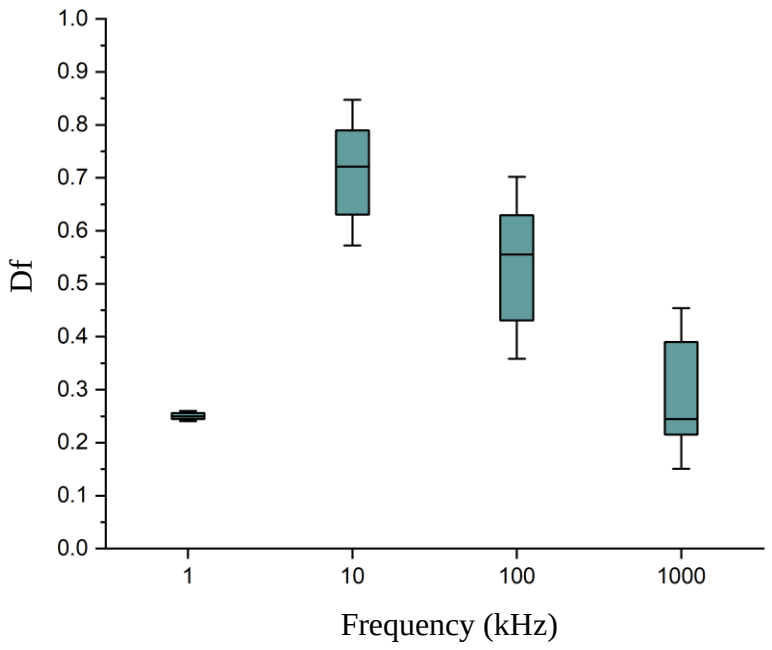

Figure 45. Variation in Df with frequency for M0.95CT-HIP ceramic.

Variation in Ɛr with frequency for M0.95CT and M0.95CT-HIP ceramics are shown in Figure 46. For each frequency, 3 measurements were made for M0.95CT and M0.95CT-HIP ceramics. The Ɛr of M0.95CT-HIP ceramic was averaged at 37.71, 33.96, 29.04, and 22.46 for 1 kHz, 10 kHz, 100 kHz, and 1 MHz, respectively.

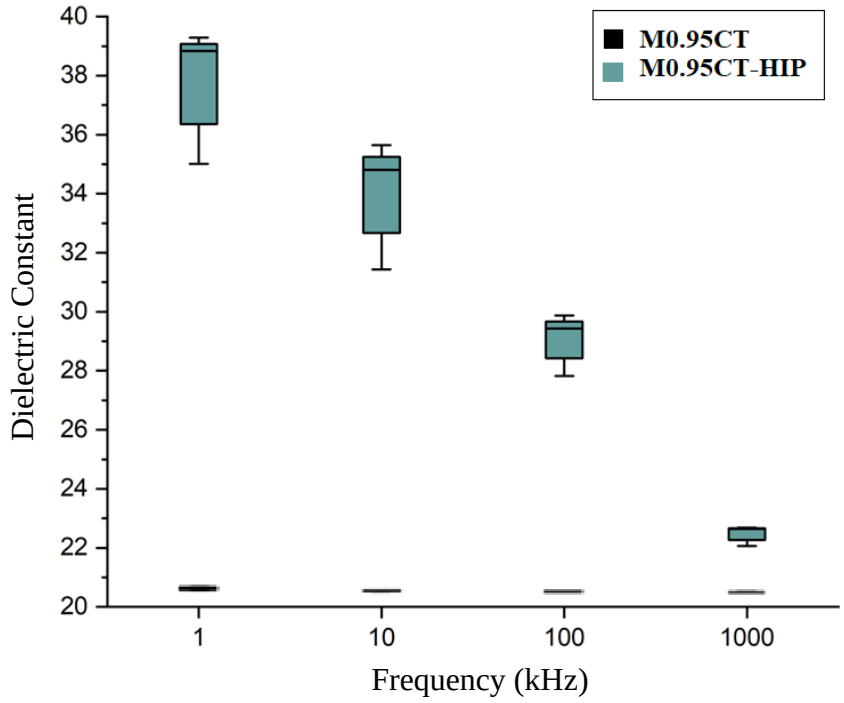

Figure 47. Variation in dielectric constant with frequency for M0.95CT and M0.95CT-HIP ceramics.

The Ɛr values of M0.95CT-HIP ceramic are higher than expected. Also, there is more scatter among data at the same and different frequencies unlike the Ɛr values of M0.95CT ceramic. These results can be interpreted as an indication of a change in the electrical properties of the ceramic with the application of HIP. In other words, HIPing affected the insulating behavior of M0.95CT ceramic. This can be explained by the fact that M0.95CT-HIP ceramic has high Ɛr and Df values that cause a decrease in dielectric properties. It can be concluded that dielectric properties of

M0.95CT ceramic are significantly influenced by the HIP application and no longer exhibits insulating behavior.

4.4.4.3 Resistivity

The variation of the resistivity of M0.95CT-HIP ceramic as measured from room temperature to 400 °C at intervals of 100 °C is shown in Figure 48. An abrupt increase was observed in conductivity with increasing temperature. Resistivity reaches to approximately 10^3 Ω.cm at 400 °C. As temperature rises, more thermal energy is available to excite electrons from the valence to the conduction band, increasing the concentrations of both electrons and holes. [64] This may be one of the main reasons why conductivity increases with increasing temperature.

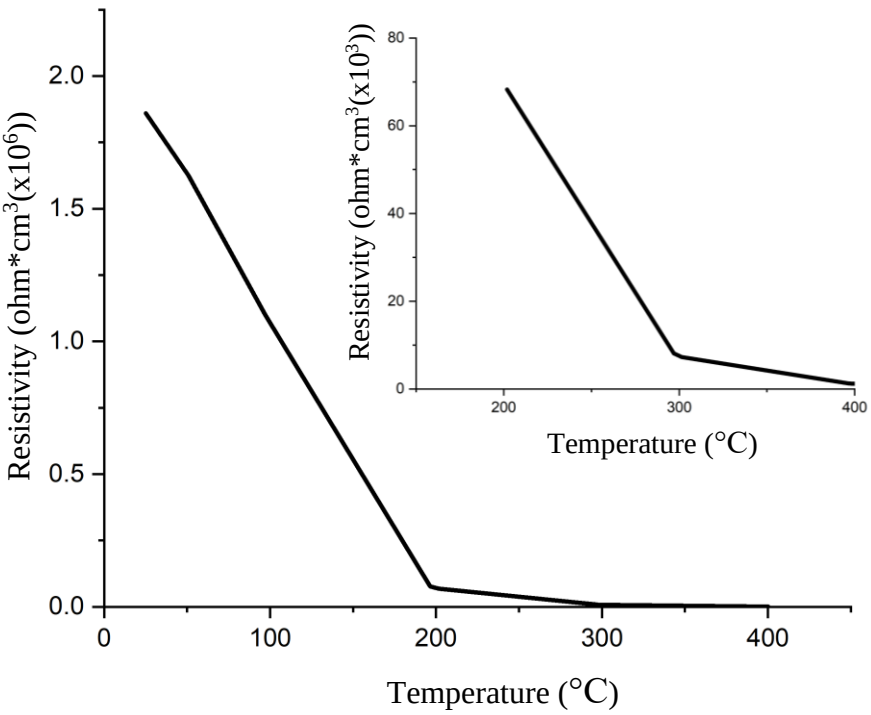

Figure 48. Resistivity of M0.95CT-HIP ceramic.

Resistivity of semiconductors ranges from 10^{-4} Ω.cm (heavily doped) to 10^{3} Ω.cm (undoped, or intrinsic). [65] According to Antonije et al. [66], HIP transforms $MgTiO_3$ ceramics into a semiconductor. This information gives a clue that a semiconductor material with high resistance was obtained in this study upon application of HIPing. It can be anticipated that M0.95CT-HIP ceramic might be used as a semiconductor in extreme operating temperature conditions.

4.4.4.4 Hall Effect

Hall potential, magnetic field, and current values were measured and used to calculate sheet carrier density. Hall mobility values were determined using the sheet resistivity, which is calculated to be 4.8×10^{5} Ω/sq. The results of the Hall effect measurement of M0.95CT-HIP ceramic at room temperature is shown in Figure 49. Hall mobility values give a clue about hole transport mechanism. As seen in Figure 49, Hall mobility values are positive.It can be concluded that holes are the majority carriers in M0.95CT-HIP ceramic. M0.95CT ceramic transforms from insulator to p-type semiconductor at room temperature upon HIPing.

The sheet carrier density values obtained in this study seem to be lower then general semiconductors. For example, the lightest doped region of a silicon device typically ranges between 10^{14} and 10^{17} cm^{-3}. [67] The carriers of M0.95CT-HIP ceramic are more mobile at 400 °C. Therefore, Hall effect measurement at temperatures higher than room temperature will be more accurate for this study. Jankowski et al. [68] supports this finding by reporting that the automotive, aerospace, military, oil, gas, and spacecraft sectors are mainly responsible for the need for the use of different technologies in extreme temperatures. Apparently, achieving a high performance at high temperatures might be considerably more challenging in the case of semiconductor devices. Therefore, Hall effect measurements are generally made depending on the temperature if adequate equipment can be provided.

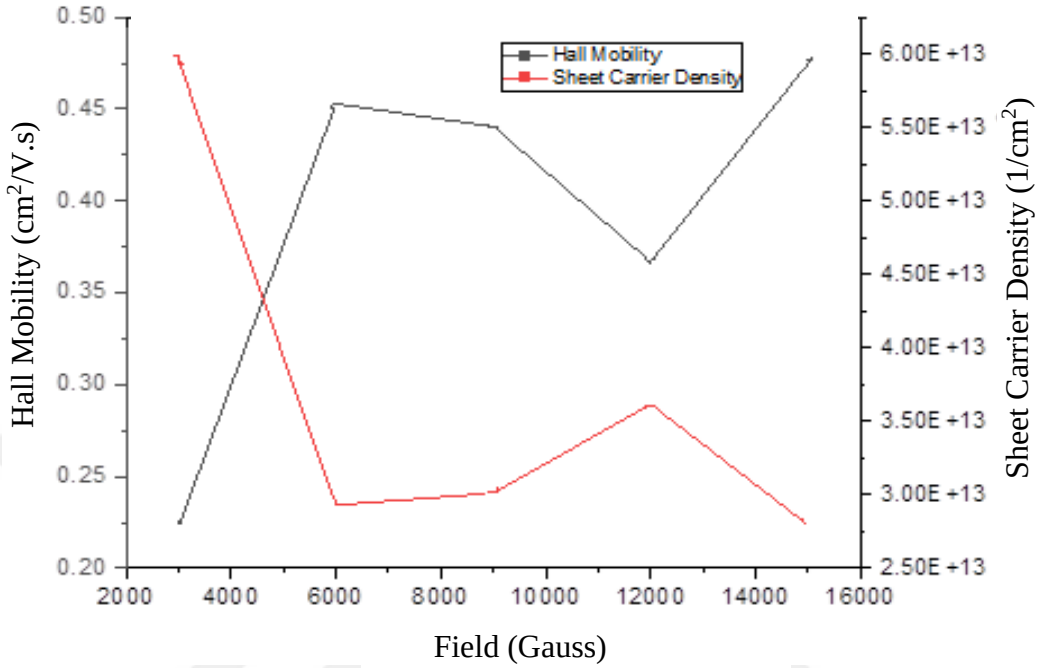

Figure 49. Hall-Effect and sheet carrier density for M0.95CT-HIP ceramic.

4.4.4.5 Absorbance

The absorption change of M0.95CT-HIP ceramic with respect to the wavelength is shown in Figure 50. Despite grinding in the mortar and dispersion in ethyl alcohol with ultrasonic stirrer, the settlement of the particles in the liquid can only be partially prevented. The reason for the initial negative absorption values in the graph may be due to particle settlement during measurement. Also, the fact that two different peaks occurred at the wavelengths of approximately 245 and 284 nm were due to the non-homogeneous dispersion of the particles. Measuring powder with smaller particle size could help to obtain a smoother graphic but, it is difficult to reduce particles to smaller size with single distribution. Doak et al. [69] suggest that even a little quantity of big particles could have a considerable impact on the absorbance spectrum of a gold nanoparticle solution. Another possible reason for the

absorption difference may be the device can not take measurements fast enough before particle settlement.

Eg of M0.95CT-HIP ceramic was calculated by using the absorbance results and Eq. (4). The smallest wavelength value in Figure 50, where the absorbance value did not change with increasing wavelength, was 458 nm. This wavelength value was used for the calculation for Eg of M0.95CT-HIP ceramic. In a narrow wavelength range, the peak is shown clearly in the inset in Figure 50.

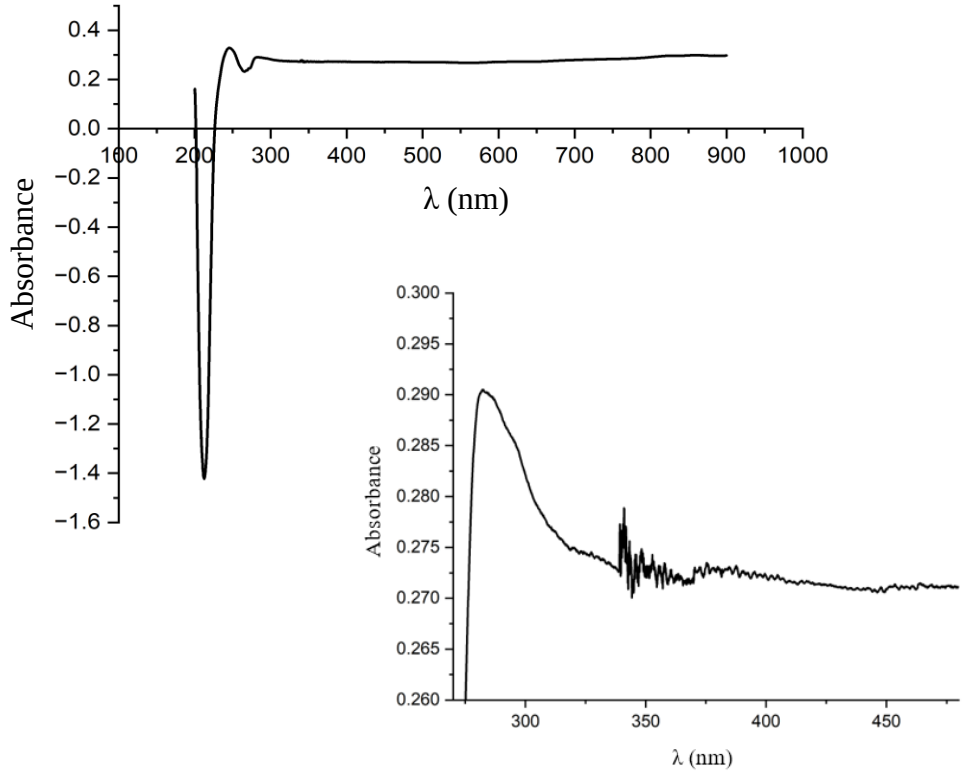

Figure 50. Absorbance with respect to wavelength for M0.95CT-HIP ceramic.

The Eg value of M0.95CT-HIP ceramic, which was determined using a Tauc plot, is shown in Figure 51. The Eg value of M0.95CT-HIP ceramic is recognized at the position where a straight line touches the x-axis, which is approximately 2.71 eV. Low et al. [70] stated that with a 5% margin of error, the value of Eg for silicon ranges from 1.13 ± 0.057 eV at 273 K to 1.11 ± 0.056 eV at 330 K. The M0.95CT-HIP ceramic has a very high Eg value compared to silicon.

Neudeck et al. [67] stated that the intrinsic carrier concentrations of semiconductors with broad bandgaps (~ 3 eV) like SiC and GaN are much lower than those of silicon. Therefore, intrinsic carrier conductivity issues do not arise until considerably higher temperatures, above 600 °C.

Jankowski et al. [68] reported that materials with a large band-gap shows good thermal stability in terms of electrical characteristics at high temperatures. Therefore, these materials should be the foundation for high temperature electronics. M0.95CT-HIP ceramic could be one of these materials as it has a wide Eg range like SiC and GaN. However, it should be considered that these materials have a weak point in that their poor electron mobility causes a reduction in the magnetic sensitivity of the sensors compared to materials with a narrow band-gap. [68]

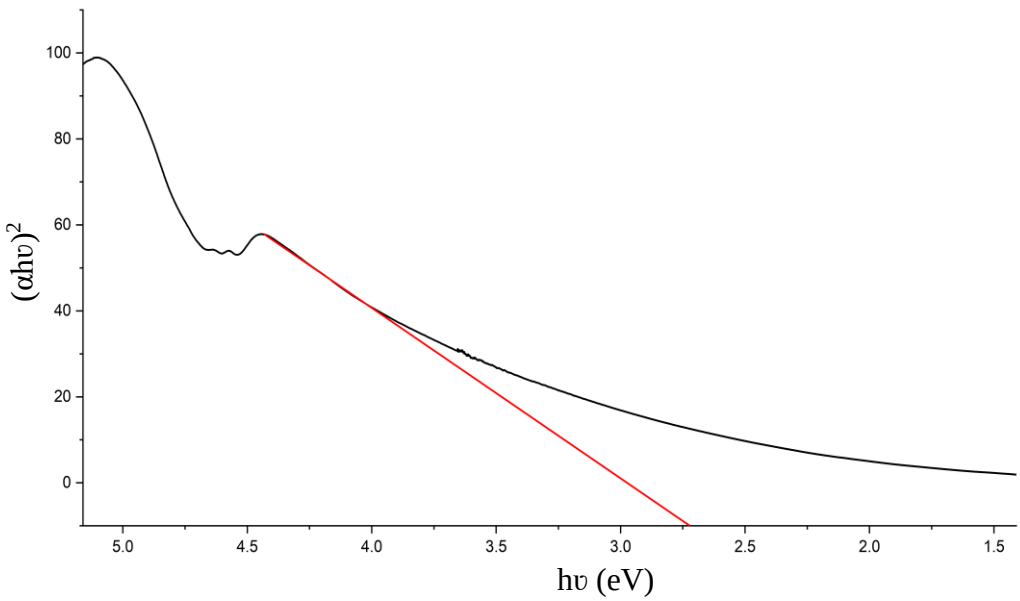

Figure 51. Determination of the Eg value of M0.95CT-HIP ceramic.

CHAPTER 5

CONCLUSION

A study of the effect of hot isostatic pressing (HIPing) on densification, microstructure, and electrical properties of $0.95MgTiO_3$-$0.05CaTiO_3$ ceramic has led to the following conclusions.

- The $0.95MgTiO_3$-$0.05CaTiO_3$ ceramic could successfully be produced by mixed oxide method.
- The M0.95CT ceramic pressureless sintered at 1400 °C, with a relative density of 96.06%, a εr value of 20.47 (at 1 MHz), and a Df value of 0.00222, performs best compared to the M0.95CT ceramics pressureless sintered at lower temperatures.
- The XRD and EDS analyses revealed that the amount of the undesirable $MgTi_2O_5$ phase decreases by applying calcination twice and by increasing the sintering temperature. However, it could not be completely eliminated in the structure.
- The dielectric properties of ceramics are influenced by and directly related to microstructural features such as grain size, second phases, and porosity.
- HIPing improves densification. The relative theoretical density of the M0.95CT ceramic pressureless sintered at 1400 °C has been improved from 96.06% to 97.2% upon HIPing.
- The addition of HIPing to the production steps of the M0.95CT ceramic changes its electrical behavior from insulator to semiconductor.
- Resistivity of M0.95CT-HIP ceramic reaches approximately to 10^3 Ω.cm at 400 °C. The electrical behavior of M0.95CT-HIP ceramic changes from insulator to semiconductor particularly at high temperatures.

- Hall effect measurement findings support resistivity results by indicating that M0.95CT-HIP ceramic is a p-type semiconductor.
- The Eg of M0.95CT-HIP ceramics is ~2.71 eV. The relatively low Eg of M0.95CT-HIP ceramic makes it attractive for high temperature applications.

CHAPTER 6

FUTURE STUDIES

It is possible to systematically test the dielectric properties at higher frequencies like microwave frequencies in terms of the Ɛr and Df values. Therefore, how the dielectric behavior of M0.95CT ceramic changes as the frequency increases can be find out.

The quantitative value of $MgTi_2O_5$ phase can be determined for M0.95CT ceramics produced at different pressureless sintering temperatures by using Rietveld analysis.

Temperature, pressure, and time optimization can be performed for the HIP process.

Resistivity measurement of M0.95CT-HIP ceramic can be performed at temperatures higher than 400 °C.

By quantitative identification of molecules using Raman Spectroscopy or XPS, it can be determined whether there is a decrease in oxygen partial pressure after HIPing.

REFERENCES

[1] M. T. Sebastian, *Dielectric Materials for Wireless Communication*, Elsevier, 2008, doi: 10.1016/B978-0-08-045330-9.X0001-5.

[2] K. Wang, H. Zhou, W. Sun, X. Chen, and H. Ruan, "Solid-state reaction mechanism and microwave dielectric properties of $0.95MgTiO_3$–$0.05CaTiO_3$ ceramics," *Journal of Materials Science: Materials in Electronics*, vol. 29, no. 3, pp. 2001–2006, Feb. 2018, doi: 10.1007/s10854-017-8111-z.

[3] Y. C. Liou and S. L. Yang, "Calcium-doped $MgTiO_3$-$MgTi_2O_5$ ceramics prepared using a reaction-sintering process," *Materials Science and Engineering B*, vol. 142, no. 2–3, pp. 116–120, Sep. 2007, doi: 10.1016/j.mseb.2007.06.027.

[4] C. Chen, Z. Peng, L. Xie, K. Bi, and X. Fu, "Microwave dielectric properties of novel $(1 - x)MgTiO_3$–$xCa0.5Sr0.5TiO_3$ ceramics," *Journal of Materials Science: Materials in Electronics*, vol. 31, no. 16, pp. 13696–13703, Aug. 2020, doi: 10.1007/s10854-020-03927-1.

[5] Z. Hou, F. Ye, and L. Liu, "Effects of pore shape and porosity on the dielectric constant of porous β-SiAlON ceramics," *Journal of the European Ceramic Society*, vol. 35, no. 15, pp. 4115–4120, Dec. 2015, doi: 10.1016/j.jeurceramsoc.2015.07.002.

[6] M. A. Sanoj, C. P. Reshmi, K. P. Sreena, and R. Varma, "Sinterability and microwave dielectric properties of nano structured $0.95MgTiO_3$-$0.05CaTiO_3$ synthesised by top down and bottom up approaches," *Journal of Alloys and Compounds*, vol. 509, pp. 3089–3095, 2011, doi: 10.1016/j.jallcom.2010.12.006.

[7] P. Cousin and R. A. Ross, "Preparation of Mixed Oxides: a Review," *Materials Science and Engineering: A*, vol. 130, no.1, pp. 119-125, 1990, doi: 10.1016/0921-5093(90)90087-J.

[8] V. S. Samyuktha, A. G. Sampath Kumar, T. S. Rao, and R. P. Suvarna, "Synthesis, structural and dielectric properties of magnesium calcium titanate (1-x)$MgTiO_3$-x$CaTiO_3$ (x=0, 0.1, 0.2 and 0.3)," in *Materials Today: Proceedings*, 2016, vol. 3, no. 6, pp. 1768–1771. doi: 10.1016/j.matpr.2016.04.072.

[9] X. Zhou, Y. Yuan, L. Xiang, and Y. Huang, "Synthesis of $MgTiO_3$ by solid state reaction and characteristics with addition," *Journal of Materials Science*, vol. 42, no. 16, pp. 6628-6632, 2007. doi: 10.1007/s10853-007-1510-4.

[10] V. M. Ferreira, F. Azough, R. Freer, and J. L. Baptista, "The effect of Cr and La on $MgTiO_3$ and $MgTiO_3$-$CaTiO_3$ microwave dielectric ceramics," 2015. [Online]. Available: http://journals.cambridge.org

[11] I. N. Jawahar, M.T. Sebastian, and P. Mohanan "Preparation, characterisation, and microwave dielectric properties of $A_nB_{n-1}O_{3n}$ (n=5,6,8) type perovskite compounds," *Materials Science*, 2002.

[12] "A. K. Mohamed, "TP3-Ceramics: Sintering and Microstructure," *Ceramics & Colloids*, 2008.

[13] S. Filipovic, V. P. Pavlovic, N. Obradovic, V. Paunovic, K. Maca, and V. B. Pavlović, "The impedance analysis of sintered $MgTiO_3$ ceramics," *Journal of Alloys and Compounds*, vol. 701, pp. 107–115, 2017, doi: 10.1016/j.jallcom.2017.01.117.

[14] Y. C. Chen, C. W. Wang, K. H. Chen, Y. da Huang, and Y. C. Chen, "Microwave dielectric properties of 0.93(Mg0.95Co0.05)TiO_3-0.07$CaTiO_3$ for application in patch antenna," *Japanese Journal of Applied Physics*, vol. 47, no. 2 PART 1, pp. 992–997, Feb. 2008, doi: 10.1143/JJAP.47.992.

[15] K. W. Tay and W. F. Wu, "Pure oxygen atmosphere sintering behavior and microwave dielectric properties of x($Mg_{0.96}Co_{0.04}$)TiO_3-(1-x)$SrTiO_3$ ceramics," in *Procedia Engineering*, 2012, vol. 36, pp. 462–467. doi: 10.1016/j.proeng.2012.03.067.

[16] K. Wakino, “Recent development of dielectric resonator materials and filters in japan,” *Ferroelectrics*, vol. 91, no. 1, pp. 69–86, Mar. 1989, doi: 10.1080/00150198908015730.

[17] V. M. Ferreira, F. Azough, R. Freer, and J. L. Baptista, “The effect of Cr and La on $MgTiO_3$ and $MgTiO_3$-$CaTiO_3$ microwave dielectric ceramics,” 1997.

[18] M. T. Sebastian, *Dielectric materials for wireless communication.* Amsterdam: Elsevier, 2008.

[19] M. E. Örek, “Dielectric property-microstructure relation in $MgTiO_3$-$CaTiO_3$ ceramics,” 2019.

[20] Y. Suzuki and Y. Shinoda, “Magnesium dititanate ($MgTi_2O_5$) with pseudobrookite structure: A review,” *Science and Technology of Advanced Materials*, vol. 12, no. 3. Jun. 2011. doi: 10.1088/1468-6996/12/3/034301.

[21] V. Daněk and I. Nerád, “Phase diagram and structure of melts of the system CaO-TiO_2-SiO_2.”

[22] C. L. Pan, C. H. Shen, W. C. Lin, and S. H. Lin, “Effect of B_2O_3 glass on the sintering and microwave dielectric properties of $MgTiO_3$–$CaTiO_3$,” in *Applied Mechanics and Materials*, 2014, vol. 666, pp. 27–30. doi: 10.4028/www.scientific.net/AMM.666.27.

[23] N. Ichinose and H. Yamamoto, “Effect of additives on microwave dielectric properties in low-temperature firing $(Mg,Ca)TiO_3$ based ceramics,” *Ferroelectrics*, vol. 201, no. 1–4, pp. 255–262, 1997, doi: 10.1080/00150199708228375.

[24] “Dielectric,” Encyclopedia Britannica. [Online]. Available: https://www.britannia.com/science/dielectric. [Accessed: 10-Jan-2023].

[25] M. Gupta and W. L. Wong, *Microwaves and metals*. John Wiley & Sons, 2007.

[26] Y. M. Poplavko, “Dielectrics,” *Electronic Materials*, Elsevier, 2019, pp. 287–408. doi: 10.1016/B978-0-12-815780-0.00007-4.

[27] K. Technologies, “Basics of measuring the dielectric properties of materials.” [Online]. Available: www.keysight.com

[28] R. Dorey, “Microstructure–property relationships,” *Ceramic Thick Films for MEMS and Microdevices*, pp. 85–112, 2012, doi: 10.1016/B978-1-4377-7817-5.00004-3.

[29] M. N. Rahaman, “Ceramic Fabrication Processes: An Introductory Overview.” *Ceramic Processing and Sintering*, New York: M. Dekker, pp. 48, 2003.

[30] A. Lisinska-Czekaj, “Fabrication of $Bi_6Fe_2Ti_3O_{18}$ ceramics by mixed oxide method,” *Materials Science Forum*, 2013, vol. 730–732, pp. 100–104. doi: 10.4028/www.scientific.net/MSF.730-732.100.

[31] N. Kumar, A. Bharti, M. Dixit, and A. Nigam, “Composite materials effect of powder metallurgy process and its parameters on the mechanical and electrical properties of copper-based materials: Literature Review,” *Powder Metallurgy and Metal Ceramics*, vol. 59, no. 8, pp. 57–68, doi: 10.1007/s11106-020-00174-1.

[32] D. Segal, “Conventional routes to ceramics,” *Chemical Synthesis of Advanced Ceramic Materials*, Cambridge University Press, 2011, pp. 17–22. doi: 10.1017/cbo9780511565014.003.

[33] D. Chaira, “Powder metallurgy routes for composite materials production,” *Encyclopedia of Materials: Composites*, Elsevier, 2021, pp. 588–604. doi: 10.1016/b978-0-12-803581-8.11703-5.

[34] P. Dayal and G. Triani, “*Hot isostatic pressing: HIP’17”. 12th international conference on hot isostatic pressing (HIP’17)*, Sydney, Australia, 5-8 December 2017.

[35] N. L. Loh and K. Y. Sia, “An overview of hot isostatic pressing,” 1992.

[36] “Techniques for measuring resistivity for materials characterization,” *Tetronix*, [Online]. Available: https://download.tek.com/document/1KW-60826-0_4200AMaterialsAppsGuide.pdf. [Accessed: 10-Jan-2023].

[37] E. N. Kaufmann, *Characterization of materials.* Wiley, 2012.

[38] T. Nehls and G. Wessolek, “Electric Resistance,” *Encyclopedia of Earth Sciences Series*, vol. Part 4, pp. 941–942, 2021, doi: 10.1007/978-90-481-3585-1.

[39] “Hall effect,” Encyclopedia Britannica. [Online]. Available: https://www.britannica.com/science/Hall-effect [Accessed: 10-Jan-2023].

[40] Z. Chen and T. F. Jaramillo, “The use of UV-visible spectroscopy to measure the band gap of a semiconductor,” pp. 18, 2017.

[41] “UV-VIS spectrometer,” *Scribd*, [Online]. Available: https://www.scribd.com/document/535219439/PH211-2019-7-UVVIS-absorption, doi: 10.1063/1.5028819, [Accessed: 10-Jan-2023].

[42] “Safety Data Sheet Revision Date 07/23/2022 version 8.” [Online]. Available: https://www.sigmaaldrich.com/TR/en/sds/sigald/534056. [Accessed: 10-Jan-2023].

[43] P. Pei, M. C. Bhardwaj, J. Anderson, D. Minor, and T. Thornton, “Instrumentation: Measuring Green Body Density”. *Ceramic Industry*, 2000.

[44] M. T. Jilani, M. Zaka, A. M. Rehman, M. T. Khan, S. Khan, and A. Muzamil, “A brief review of measuring techniques for characterization of dielectric materials,” 2012.

[45] C. L. Huang and M. H. Weng, “Improved high Q value of $MgTiO_3$-$CaTiO_3$ microwave dielectric ceramics at low sintering temperature,” 2001.

[46] G. Balakrishnan, R. Velavan, K. Mujasam Batoo, and E. H. Raslan, "Microstructure, optical and photocatalytic properties of MgO nanoparticles," *Results Phys*, vol. 16, Mar. 2020, doi: 10.1016/J.RINP.2020.103013.

[47] S. B. Choi, N. W. Kim, D. K. Lee, and H. Yu, "Growth mechanism of cubic MgO granule via common ion effect," *J Nanosci Nanotechnol*, vol. 13, no. 11, pp. 7577–7580, Nov. 2013, doi: 10.1166/JNN.2013.7882.

[48] P. Srinivasu, S. P. Singh, A. Islam, and L. Han, "Novel approach for the synthesis of nanocrystalline anatase titania and their photovoltaic application," *Adv Optoelectron*, vol. 2011, 2011, doi: 10.1155/2011/539382.

[49] D. Render, T. Samuel, H. King, M. Vig, S. Jeelani, R. J. Babu, and V. Rangari, "Biomaterial-Derived Calcium Carbonate Nanoparticles for Enteric Drug Delivery," *Journal of Nanomaterials*, vol. 2016, 2016, doi: 10.1155/2016/3170248.

[50] L. Wang, G. Yang, S. Peng, J. Wang, D. Ji, W. Yan, and S. Ramakrishna, "Fabrication of $MgTiO_3$ nanofibers by electrospinning and their photocatalytic watersplitting activity," *International Journal of Hydrogen Energy*, vol. 42, no. 41, pp. 25882–25890, Oct. 2017, doi: 10.1016/j.ijhydene.2017.08.194.

[51] C. Han, J. Liu, W. Yang, Q. Wu, H. Yang, and X. Xue, "Photocatalytic activity of $CaTiO_3$ synthesized by solid state, sol–gel and hydrothermal methods," *Journal of Sol-Gel Science and Technology*, vol. 81, no. 3, pp. 806–813, Mar. 2017, doi: 10.1007/s10971-016-4261-3.

[52] Y. Nakagoshi and Y. Suzuki, "Morphology control of pseudobrookite-type $MgTi_2O_5$ powders by LiF doping," *International Letters of Chemistry, Physics and Astronomy*, vol. 46, pp. 37–41, Jan. 2015, doi: 10.18052/www.scipress.com/ilcpa.46.37.

[53] Libretext, “8.2: Atomic and Ionic Radius - Chemistry LibreTexts.” https://chem.libretexts.org/Courses/Bellarmine_University/BU%3A_Chem_ [Accessed:10-Jan-2023].

[54] Y. Yu, Y. Wang, W. Guo, C. Zhu, A. Ji, H. Wu, S. Liang, S. Xiong, and X. Wang, “Grain size engineered 0.95$MgTiO_3$–0.05$CaTiO_3$ ceramics with excellent microwave dielectric properties and prominent mechanical performance,” *Journal of the American Ceramic Society*, vol. 105, no. 1, pp. 299–307, Jan. 2022, doi: 10.1111/JACE.18045.

[55] U. Täffner, V. Carle, and U. Schäfer, “Preparation and Microstructural Analysis of High-Performance Ceramics,” 2004, Accessed: Oct. 24, 2022. [Online]. Available: www.asminternational.org

[56] J. Konopka and T. F. Scientific, “Options for Quantitative Analysis of Light Elements by SEM/EDS.”

[57] V. M. Ferreira, F. Azough, R. Freer, and J. L. Baptista, “The effect of Cr and La on $MgTiO_3$ and $MgTiO_3$-$CaTiO_3$ microwave dielectric ceramics,” 2015. [Online]. Available: http://journals.cambridge.org

[58] C. L. Huang, P. E. Chiang, and T. H. Hsu, “Influence of intrinsic and extrinsic factors on microwave dielectric properties of $(Sr(1-x)Mg(x))V_2O_6$ (x=0.01-0.09) ceramics for ULTCC applications,” 2021, doi: 10.1016/j.mseb.2021.115438.

[59] C. L. Huang and M. H. Weng, “Improved high Q value of $MgTiO_3$-$CaTiO_3$ microwave dielectric ceramics at low sintering temperature,” 2001.

[60] M. Qasim, A. Naseeb, I. Ahmad, G. Mustafa, M. T. Farid, M. Kanwal, A. Ali, G Abbas, G. Murtaza, M. A. Khan, M. H. Aziz, S. M. Ali, M. R. Baig, T. S. Alkhuraiji, and M. Ahmad, “Synthesis, structural and high frequency dielectric properties of polypyrrole (PPy)/holmium ferrite composites,” *Journal of Materials Science: Materials in Electronics*, vol. 29, no. 5, pp. 3884–3890, Mar. 2018, doi: 10.1007/s10854-017-8326-z.

[61] "Volume Resistivity," Precision Ceramics USA. Available: https://precision-ceramics.com/materials/properties/volume-resistivity. [Accessed: 10-Jan-2023].

[62] M. Hu, Z. Ding, Z. Zeng, D. Ji, and C. Luo, "A miniaturized microwave bandpass filter based on modified (Mg0.95Ca0.05)TiO_3 substrate", doi: 10.1051/02003.

[63] S. Filipovic, N. Obradovic, V. B. Pavlovic, M. Mitric, A. Dordevic, M. Kachlik, and K. Maca, "Effect of consolidation parameters on structural, microstructural and electrical properties of magnesium titanate ceramics," *Ceramics International*, vol. 42, no. 8, pp. 9887–9898, Jun. 2016, doi: 10.1016/j.ceramint.2016.03.088.

[64] W. D. Callister and D. G. Rethwisch, "Materials Science and Engineering, 9th Edition," *Wiley*.

[65] "Conductivity," Microwaves101Conductivity. [Online] Available: https://www.microwaves101.com/encyclopedias/conductivity. [Accessed: 10-Jan-2023].

[66] D. Antonije, R. D. I. Olcan, N. Obradovic, V. Paunovic, S. Filipovic, and V. B. Pavlovic, "Electrical properties of magnesium titanate ceramics post-sintered by hot isostatic pressing," *Science of Sintering*, vol. 49, no. 4, pp. 373–380, 2017, doi: 10.2298/SOS1704373D.

[67] P. G. Neudeck, R. S. Okojie, and L. Y. Chen, "High-temperature electronics - A role for wide bandgap semiconductors?," *Proceedings of the IEEE*, vol. 90, no. 6, pp. 1065–1076, 2002, doi: 10.1109/JPROC.2002.1021571.

[68] J. Jankowski, S. El-Ahmar, and M. Oszwaldowski, "Hall sensors for extreme temperatures," *Sensors*, vol. 11, no. 1, pp. 876–885, Jan. 2011, doi: 10.3390/S110100876.

[69] J. Doak, R. K. Gupta, K. Manivannan, K. Ghosh, and P. K. Kahol, “Effect of particle size distributions on absorbance spectra of gold nanoparticles,” *Physica E: Low-dimensional Systems and Nanostructures*, vol. 42, no. 5, pp. 1605–1609, Mar. 2010, doi: 10.1016/j.physe.2010.01.004.

[70] J. Low, M. Kreider, D. Pulsifer, A. Jones, and T. Gilani, “Band Gap Energy in Silicon,” *American Journal of Undergraduate Research*, vol. 8, no. 2 and 3, Dec. 2009, doi: 10.33697/ajur.2009.017.

[71] A. J. Moulson and J. M. Herbert, *Electroceramics: Materials, properties, applications*. 1990.